# Exclusive Compton Scattering
# on the Proton

J.P. Chen[1], E. Chudakov[1], C. DeJager[1], P. Degtyarenko[1], R. Ent[1], J. Gomez[1], O. Hansen[1],
C. Keppel[1], F. Klein[1], M. Kuss[1], J. LeRose[1], M. Liang[1], R. Michaels[1], J. Mitchell[1],
N. Liyanage[1], P. Rutt[1], A. Saha[1], B. Wojtsekhowski[1], M. Bouwhuis[2], T.H. Chang[2], R.J. Holt[2],
A.M. Nathan[2], M. Roedelbronn[2], K. Wijesooriya[2], S.E. Williamson[2], G. Dodge[3], C. Hyde-Wright[3], A. Radyushkin[3], F. Sabatie[3], L.B. Weinstein[3], P. Ulmer[3], P.E. Bosted[4], J.M. Finn[5],
M. Jones[5], S. Churchwell[6], C. Howell[6], R. Gilman[7], C. Glashausser[7], X. Jiang[7], R. Ransome[7],
S. Strauch[7], J. Berthot[8], P. Bertin[8], H. Fonvieille[8], Y. Roblin[8], W. Bertozzi[9], S. Gilad[9], D.
Rowntree[9], Z. Zu[9], D. Brown[10], G. Chang[10], A. Afanasev[11], K. Egiyan[12], E. Hoohauneysan[12],
A. Ketikyan[12], S. Mailyan[12], A. Petrosyan[12], A. Shahinyan[12], H. Voskanyan[12], W. Boeglin[13],
P. Markowitz[13], J. Hines[14], G. Strobel[14], J. Templon[14], G. Feldman[15], C.L. Morris[16],
V. Gladyshev[17], R.A. Lindgren[17], J. Calarco[18], W. Hersman[18], M. Leuschner[18], A.Gasparian[19],
**and The Jefferson Lab Hall A Collaboration**

[1] *Thomas Jefferson National Accelerator Facility, Newport News, Virginia 23606*
[2] *Department of Physics, University of Illinois, Urbana, Illinois, 61801*
[3] *Old Dominion University, Norfolk, Virginia 23508*
[4] *The American University, Washington, D.C. 20016*
[5] *College of William and Mary, Williamsburg, Virginia 23187*
[6] *Duke University, Durham, North Carolina 27706*
[7] *Rutgers, The State University of New Jersey, Piscataway, New Jersey 08855*
[8] *Laboratoire de Physique Corpusculaire, IN2P3-CNRS,*
   *Université Blaise Pascal, F-63177 Aubière, France*
[9] *Massachusetts Institute of Technology, Cambridge, Massachusetts 02139*
[10] *University of Maryland, College Park, Maryland 20742*
[11] *North Carolina Central University, Durham, North Carolina 27707*
[12] *Yerevan Physics Institute, Yerevan 375036, Armenia*
[13] *Florida International University, Miami, Florida 33199*
[14] *University of Georgia, Athens, Georgia 30602*
[15] *George Washington University, Washington, D.C. 20052*
[16] *Los Alamos National Laboratory, Los Alamos, USA*
[17] *University of Virginia, Charlottesville, Virginia 22901*
[18] *University of New Hampshire, Durham, New Hampshire 03824*
[19] *Hampton University, Hampton, Virginia 23668*

**3 1 - 0 4**

**PCCF RI 9917**

# Exclusive Compton Scattering
# on the Proton

J. P. Chen, E. Chudakov, C. DeJager, P. Degtyarenko, R. Ent,J. Gomez, O. Hansen, C. Keppel,
F. Klein, M. Kuss, J. LeRose, M. Liang, R. Michaels, J. Mitchell, N. Liyanage, P. Rutt, A. Saha,
B. Wojtsekhowski (co-spokesman and contact person)
*Jefferson Laboratory*

M. Bouwhuis, T-H Chang, R. J. Holt, A. M. Nathan (co-spokesman), M. Roedelbronn,
K. Wijesooriya, S. E. Williamson
*University of Illinois at Urbana-Champaign*

G. Dodge, C. Hyde-Wright (co-spokesman), A. Radyushkin, F. Sabatie, L. B. Weinstein, P. Ulmer
*Old Dominion University*

P. Bosted
*The American University*

J. M. Finn, M. Jones
*College of William and Mary*

S. Churchwell, C. Howell
*Duke University*

R. Gilman, C. Glashausser, X. Jiang, R. Ransome, S. Strauch
*Rutgers University*

J. Berthot, P. Bertin, H. Fonvielle, Y. Roblin
*University Blaise Pascal/IN2P3*

W. Bertozzi, S. Gilad, D. Rowntree, Z. Zu
*Massachusets Institute of Technology*

D.Brown, G. Chang
*University of Maryland*

A. Afanasev
*North Carolina Central University*

K. Egiyan, E. Hoohauneysan, A. Ketikyan, S. Mailyan, A. Petrosyan, A. Shahinyan,
H. Voskanyan
*Yerevan Physics Institute*

W. Boeglin, P. Markowitz
*Florida International University*

J. Hines, G. Strobel, J. Templon
*University of Georgia*

G. Feldman
*George Washington University*

C. L. Morris
*Los Alamos National Laboratory*

V. Gladyshev, R. A. Lindgren
*University of Virginia*

J. Calarco, W. Hersman, M. Leuschner
*University of New Hampshire*

A. Gasparian
*Hampton University*

and

The Hall A Collaboration

(June 8, 1999)

### Abstract

An experiment is proposed to measure the cross sections for Real Compton Scattering from the proton in the energy range 3-6 GeV and over a wide angular range, and to measure the longitudinal and transverse components of the polarization transfer to the recoil proton at a single kinematic point. Together, these measurements will test models of the reaction mechanism and determine new structure functions of the proton that are related to the same nonforward parton densities that determine the elastic electron scattering form factors and the parton densities. The experiment utilizes an untagged bremsstrahlung photon beam and the standard Hall A cryogenic targets. The scattered photon is detected in a photon spectrometer, currently under construction. The coincident recoil proton is detected in one of the Hall A magnetic spectrometers and its polarization components are measured in the existing Focal Plane Polarimeter. This proposal extends and supercedes E97-108 which was approved by PAC13.

# 1 Introduction

Compton scattering in the hard scattering limit is a powerful probe of the short-distance structure of the nucleon. It is a natural complement to high $Q^2$ elastic electron scattering, where the common feature is a hard energy scale. For Real Compton Scattering (RCS), the hard scale is achieved when $s$, $-t$, and $-u$ are all large compared to the proton mass, or equivalently, when the transverse momentum transfer $p_\perp$ is large. This leads to a factorization of the transition amplitude into the convolution of a perturbative hard scattering amplitude, which involves the coupling of the external photons to the active quarks, with an overlap of initial and final soft (nonperturbative) wave functions, which describes the coupling of the active quarks to the proton. Schematically this can be written

$$T_{if}(s,t) \quad = \quad \Psi_f \otimes K(s,t) \otimes \Psi_i, \tag{1}$$

where $K(s,t)$ is the perturbative hard scattering amplitude, and $\Psi$ is the soft wave function. Three distinct theoretical approaches have been applied to RCS in recent years and these can be distinguished by the number of active constituents participating in the hard scattering subprocess. These are the so-called pertubative QCD (pQCD) mechanism [1, 2, 3] which involves three active constituents; the diquark mechanism [4, 5] which involves two; and the soft overlap mechanism [6, 7] which involves one. In any given kinematic regime, all such mechanisms will contribute, in principle, to the scattering amplitude. At "sufficiently high" energy, the pQCD mechanism will dominate, but it is not known how high is sufficiently high or the manner in which the transition to the purely pQCD mechanism emerges. At sufficiently low energy (e.g., in the resonance region), RCS is dominated by purely soft physics, and the amplitude does not factorize into hard and soft processes. At high energy but small $-t$ or $-u$, soft physics also dominates through diffractive mechanisms. The nature of the transition from purely soft to the factorization regime is not well known. Despite this uncertainty, there is a clear theoretical suggestion that at energies appropriate to JLab, factorization is valid and that the reaction is dominated by the soft overlap mechanism [6, 8].

Quite aside from the hard scattering mechanism, it is of interest to ask what RCS can teach us about the nonperturbative structure of the proton and to relate it to that revealed in other reactions. There has been much theoretical progress in recent years in providing a unified description of inclusive and exclusive reactions in the hard scattering regime [9, 10]. This is based on the concept of non-forward parton densities (ND), which are superstructure of the nucleon from which can be derived the normal parton densities, elastic form factors, and other quantities that have yet to be measured, including new form factors accessible through Compton scattering.

Despite the intense recent theoretical activity, there has been no experimental activity in this area in the last 20 years. The only Compton scattering data available in this kinematic regime are those of Shupe *et al.*[11] from Cornell, but the data in the theoretically interesting range of high $s$ *and* high $-t$ are sparse and of limited statistical precision. In order to provide the high quality data necessary to discriminate among reaction mechanisms and gain new insight into the structure of the proton, we propose an extensive program of RCS from the proton over a broad range of $s$ and $t$ accessible at JLab. The experiments primarily measure unpolarized cross sections; additionally a single measurement of the longitudinal and transverse components of the polarization transfer is proposed. At all points, we will make measurements with at least 5% statistical precision (including all background subtractions) and 6% systematic errors.

The proposal is organized as follows. In Section 2 we present the physics motivation and in Section 3, the experimental aspects, including the necessary equipment, expected counting rates,

backgrounds, and systematic errors. The specific request for beam time is presented in Section 4. This proposal extends and supercedes E97-108, which was approved by PAC13.

# 2  Physics Motivation

## 2.1  Overview

In view of the remarks in the Introduction, we consider several interesting questions that motivate us to develop an experimental program of wide-angle real Compton scattering at JLab:

1. At what kinematic scale is factorization into hard and soft processes valid?

2. What is the dominant hard scattering mechanism at JLab energies?

3. What insights into the structure of the proton can be learned from new and precise RCS measurements?

4. What is the relationship between structure revealed from RCS and that from other reactions, such as elastic form factors, parton densities, etc.?

We concentrate our discussion on the pQCD and soft overlap mechanisms, since these represent the two extreme views of the hard scattering process.

## 2.2  pQCD Mechanism

In the pQCD mechanism, shown schematically in Fig. 1-a, there are three active quarks and the transferred momentum is shared among them by the exchange of two hard gluons. This leads naturally to the asymptotic quark counting rule and scaling [12],

$$\frac{d\sigma}{dt} = \frac{f(\theta_{cm})}{s^n}, \tag{2}$$

where n=6 for RCS. Higher Fock states require additional gluon exchanges and are therefore suppressed by additional factors of $1/s$. For the pQCD mechanism, Eq. 1 takes the schematic form

$$T^{\mu\nu}(s,t) = \int d^3x d^3y \phi(x) \hat{K}^{\mu\nu}(x,y,s,t) \phi(y), \tag{3}$$

where $\hat{K}^{\mu\nu}(x,y,s,t)$ is the hard scattering amplitude that includes all distinct diagrams in which two photons couple to three quarks which exchange two perturbative gluons. The soft physics is contained in $\phi(x_1,x_2,x_3)$, the valence quark distribution amplitude (DA), which is related to the 3-quark light-cone wave function of the proton and from which the parton densities can be obtained. Vanderhaeghen [3] has outlined a procedure of parametrizing the DA as a sum of polynomials, with coefficients adjusted to fit RCS data. Therefore, in the kinematic regime where the pQCD mechanism dominants, precise measurements of RCS cross sections can determine the DA.

Experimentally, the Cornell data [11] support scaling with $n \approx 6$ (see Fig. 2 and 3), albeit with modest statistical precision. Nevertheless, this does not necessarily mean that pQCD is the dominant mechanism. Indeed, as shown in Fig. 2, when Eq. 3 is evaluated with the symmetric DA, $\phi \sim x_1 x_2 x_3$, the cross section badly underpredicts the data. A similar story holds for the proton elastic form factor, where the symmetric or even slightly asymmetric DA's lead to a form factor
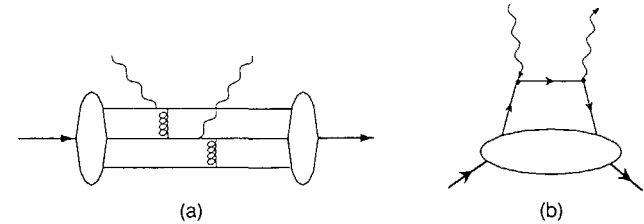


Figure 1: *Different hard scattering mechanisms for RCS. The small dots represent hard scatterings whereas the blobs represent soft interactions. In the pQCD mechanism (a), the momentum is shared among the quarks by hard gluon exchange. In the handbag diagram of (b), the scattering is from a single quark and the momentum is shared by the overlap of the high momentum components of the soft wave function.*

well below the data [8]. This can be alleviated somewhat using strongly asymmetric DA's [3], as shown in Fig. 2. However, in this case the integral is dominated by the endpoints, corresponding to the exchanged gluons close to their mass shell and therefore nonperturbative. This calls into question the internal consistency of the pQCD approach at moderate $s$ and $t$ [6, 8].

We propose to test whether the pQCD mechanism is the dominant one in the kinematic range accessible to JLab in two different ways. First, we propose precise measurements of the scaling factor $n(\theta)$, especially in the region near $\theta=90°$, since that is where $p_\perp$ is largest and therefore where the pQCD mechanism might be expected to work best. Our expected precision is shown in Fig. 3 for the angles 70°, 90°, and 110°. Second, we propose a single measurement of the longitudinal polarization transfer parameter $A_{LL}$, but we postpone a discussion of this until Sec. 2.4.

## 2.3  Soft Overlap (Handbag) Mechanism

Radyushkin [6] and subsequently Diehl *et al.* [7] suggest that the dominant mechanism at experimentally accessible energies for both elastic form factors and RCS is the soft overlap mechanism, where the handbag diagram (see Fig. 1-b) dominates and $t$ is absorbed on a single quark and shared by the overlap of high momentum components in the soft wave function. The important nonperturbative physics is contained in the wave function describing how the active quark couples to the proton. Radyushkin describes this coupling with four nonforward parton densities (ND): $\mathcal{F}^a(x;t)$, $\mathcal{G}^a(x;t)$, $\mathcal{K}^a(x;t)$, and $\mathcal{P}^a(x;t)$, corresponding to vector, axial vector, tensor, and pseudoscalar couplings, where $a$ labels the quark flavor. The ND is the superstructure that links inclusive (e.g., parton densities) to exclusive (e.g., elastic form factors) structure. For example

$$F_1(t) = \Sigma_a e_a \int_0^1 \mathcal{F}^a(x;t) dx$$
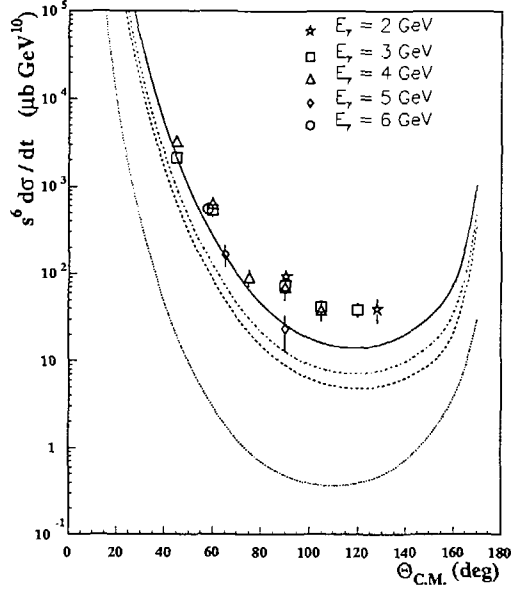
$$G_A(t) = \Sigma_a e_a \int_0^1 \mathcal{G}^a(x;t) dx$$

4

5

Figure 2: *Real Compton scattering data of Shupe[11] and pQCD calculations [1, 14, 3] using various distribution amplitudes $\phi$ for the proton structure. Solid line: KS[17], dot-dashed line: COZ[18], dashed: CZ[19], and dotted: asymptotic DA. The cross sections are multiplied by $s^6$, so that if asypmtotic scaling works, the plotted data depend only on $\theta_{cm}$.*

$$F_2(t) = \Sigma_a e_a \int_0^1 \mathcal{K}^a(x;t)dx \qquad (4)$$

and

$$f_a(x) = \mathcal{F}^a(x, t = 0)$$
$$\Delta f_a(x) = \mathcal{G}^a(x, t = 0), \qquad (5)$$

where $F_1$, $G_A$, and $F_2$ are the Dirac, Axial, and Pauli form factors, respectively and $f_a$ and $\Delta f_a$ are the spin-independent and spin-dependent parton densities, respectively. The parton density corresponding to $\mathcal{K}^a$ is not directly observable in deep inelastic scattering. Compton scattering allows access to new structure functions, such as

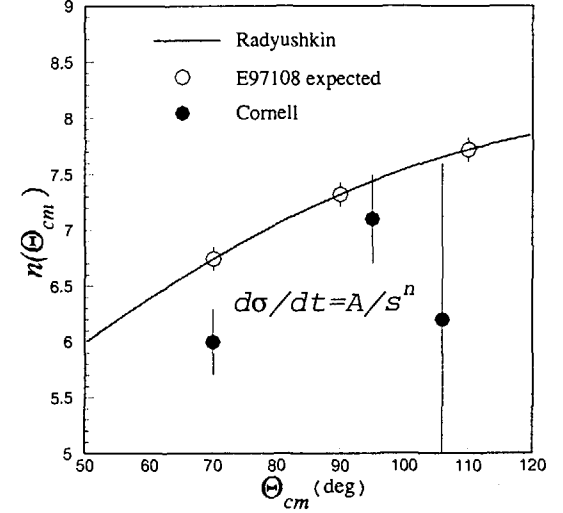$$R_V(t) = \Sigma_a e_a^2 \int_0^1 \mathcal{F}^a(x;t)\frac{dx}{x}$$



Figure 3: *Scaling of RCS cross section at fixed $\theta_{cm}$. The closed points are the Cornell data. The open points represent the projected precision from the present proposal. The curve is the prediction of Radyushkin, assuming dominance of the handbag diagram. For the pQCD mechanism, $n=6$ independent of $\theta_{cm}$.*

$$R_A(t) = \Sigma_a e_a^2 \int_0^1 \mathcal{G}^a(x;t)\frac{dx}{x}$$
$$R_T(t) = \Sigma_a e_a^2 \int_0^1 \mathcal{K}^a(x;t)\frac{dx}{x}. \qquad (6)$$

One of the primary motivations of this proposal is to measure these new structure functions.

In order to relate the RCS cross section to these new structure functions, it is necessary to make several approximations in treating the quark propagator in the hard scattering subprocess. In addition, terms involving hadron helicity flip are not treated, so that only the form factors $R_V$ and $R_A$ appear, and in particular the form factor $R_T$, which is related to $F_2$, has been neglected in treatments thus far. We will remark below on a possible experimental test of this hypothesis. With these approximations, the handbag diagram leads to the factorization of the RCS cross section into a simple product of the Klein-Nishina (KN) cross section describing the hard scattering from a single quark and a sum of form factors depending only on $t$ [6, 7]:

$$\frac{d\sigma}{d\sigma_{KN}} = f_V R_V^2(t) + (1 - f_V)R_A^2(t), \qquad (7)$$

where $f_V$ is a kinematic factor given by

$$f_V = \frac{(\tilde{s} - \tilde{u})^2}{2(\tilde{s}^2 + \tilde{u}^2)} \tag{8}$$

and $\tilde{s} = s - m^2$ and $\tilde{u} = u - m^2$. As remarked above, the new physics is contained in the form factors, $R_V$ and $R_A$, which have a simple physical interpretation. The combination $|R_V(t) + R_A(t)|^2$ is the probability that a photon can scatter elastically from the proton by transferring $t$ to a single active quark whose helicity is oriented in the direction of the proton helicity. Similarly $|R_V(t) - R_A(t)|^2$ is the probability that the active quark has helicity opposite to that of the proton. Eq. 7 is analagous to the cross section for elastic electron scattering, except that the KN cross section replaces the Mott cross section. An interesting feature is that despite the similarity between the Compton scattering form factors (Eq. 6) and electron scattering form factors (Eq. 4), there are important distinctions. First, the weighting by the quark charge is quadratic in the former case and linear in the latter. Thus RCS is sensitive to the flavor structure of the proton in a different way than electro-weak scattering, thereby potentially providing another tool, along with parity-violating electron scattering, for decomposing the flavor structure. Second, the RCS form factors have an additional $1/x$ in the integral, giving rise both to a different weighting of momentum fraction and to an overall enhancement relative to the electron scattering form factors. Both the $e_a^2$ weighting and the $1/x$ factor lead to a sensitivity to sea quarks that is greater for RCS than for electron scattering form factors. Another interesting feature is the sensitivity of RCS to the axial structure of the nucleon through $R_A$, which is a topic of high current interest in the context of the flavor decomposition of the spin-dependent structure functions.

Radyushkin and Diehl et al. have modeled the ND's in order to predict cross sections. In their models

$$\mathcal{F}^a(x,t) = f_a(x) \exp\left[\frac{(1-x)t}{4x\lambda_a^2}\right]$$

$$\mathcal{G}^a(x,t) = \Delta f_a(x) \exp\left[\frac{(1-x)t}{4x\lambda_a^2}\right], \tag{9}$$

where the factor $\lambda_a$ is related to the average transverse momentum $< k_\perp^2 >$ carried by the quarks of flavor $a$ in the proton. The helicity flip ND's $\mathcal{K}^a$ and $\mathcal{P}^a$ have not yet been modeled. Radyushkin [6] finds good agreement with the $F_1(t)$ data for $-t$ in the range 1-10 GeV$^2$ by adjusting $\lambda_a^2$ to 0.7 GeV$^2$, implying $< k_\perp^2 >\approx (300 \text{ MeV})^2$. This allows a prediction for the RCS form factors, which are shown in Fig. 4. An interesting feature of these form factors is that they decrease approximately as $1/t^2$ in the few-10 GeV$^2$ range, leading to $n \approx 6$ scaling factor, in agreement with asymptotic scaling. However, the handbag treatment of factorization predicts non-trivial violations of $n = 6$ scaling in the form of an angle-dependent scaling factor $n(\theta_{cm})$, which are in agreement with the existing (limited) data but which will be tested with good precision in the proposed experiment. Another intersting feature is that at sufficiently high $-t$, the exponential factor forces the integrand to be concentrated near $x = 1$, where the the parton distribution functions vary approximately as $(1 - x)^3$. This is the so-called Feynman mechanism [13] and it leads to an asymptotic behavior of $1/t^4$ for the form factors and therefore to $n \approx 10$. Thus the handbag contribution to RCS will be asymptotically subdominant to the hard gluon mechanism, even though the handbag is still expected to dominate at experimentally accessible energies.

In order to measure $R_V$ and $R_A$, it is necessary to measure the RCS cross section at fixed $t$ with a variable $f_V$ in order to achieve a "Rosenbluth-like" separation. Note that $f_V$, which assumes
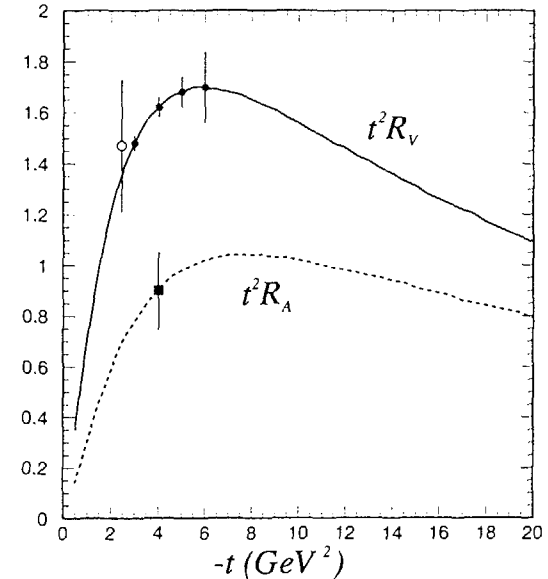
Figure 4: Calculations of the RCS form factors $t^2R_V(t)$ (solid line) and $t^2R_A(t)$ (dashed line). The closed points and error bars show the projected precision from the present proposal. The open point is the result of a fit to the Cornell data. The square is the projected precision for $R_A$ based on the measurement of $A_{LL}$.

values between about 0.5 and 1, depends principally on the scattering angle $\theta_{cm}$ and only weakly on energy, as shown in Fig. 5. For the kinematics of interest, where $s$, $-t$, and $-u$ are all large, $f_V$ is always close to 1. Consequently the unpolarized cross sections are largely insensitive to $R_A$. This leads to the very nice feature that the left-hand-side of Eq. 7 is nearly $s$-independent at fixed $t$, allowing a very powerful test of the reaction mechanism that we propose to test. In addition, the cross sections should allow a precise measurement of $R_V$, although $R_A$ will be nearly unconstrained. These features are demonstrated in Fig. 6, which shows data expected from this experiment. Also shown are the limited Cornell data at $-t=2.45$ GeV$^2$, which is probably at the edge of validity of the reaction mechanism.

## 2.4 Polarization Observables

A measurement of polarization observables provides further tests of the reaction mechanism as well as access to additional form factors. In this section we discuss the observables $A_{LL}$, $A_{LT}$, and
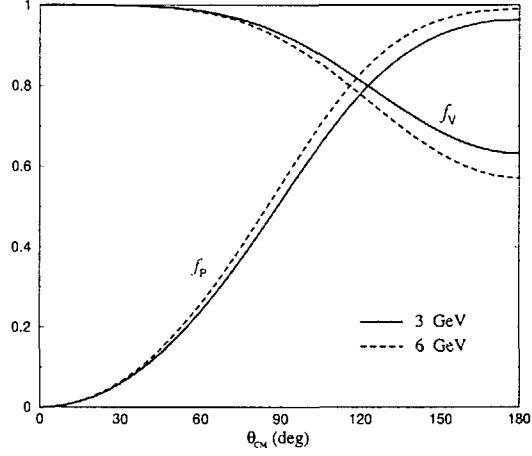
Figure 5: *Variation of the kinematic factors $f_V$ and $f_P$ with $\theta_{cm}$ at 3 (solid) and 6 (dashed) GeV.*

$P_N$.

The longitudinal polarization transfer observable $A_{LL}$ is defined by

$$A_{LL}\frac{d\sigma}{dt} \equiv \frac{d\sigma(\uparrow\uparrow)}{dt} - \frac{d\sigma(\uparrow\downarrow)}{dt} \qquad (10)$$

where the first arrow refers to the incident photon helicity and the second to the recoil proton helicity. In the handbag mechanism, this is related to the form factors by the expression [7]

$$A_{LL}\frac{d\sigma}{d\sigma_{KN}} = f_P R_V(t) R_A(t), \qquad (11)$$

where $f_P$ is a kinematic factor

$$f_P = \frac{\tilde{s}^2 - \tilde{u}^2}{\tilde{s}^2 + \tilde{u}^2}. \qquad (12)$$

Assuming the unpolarized cross section is dominated by $R_V$, then one obtains the approximate expression

$$R_A(t) \approx \frac{f_V}{f_P} R_V(t) A_{LL}. \qquad (13)$$

The structure of Eq. 11 is very interesting since it is closely related to the comparable result for Compton scattering from a point Dirac particle in the limit E≫m. In such a case, $\sigma = \sigma_{KN}$ and $R_V = R_A = 1$, so that $A_{LL} = f_P$. This quantity is plotted in Fig 5, where one sees that it vanishes in the forward direction, it is +1 in the backward direction, it is always positive, and it is
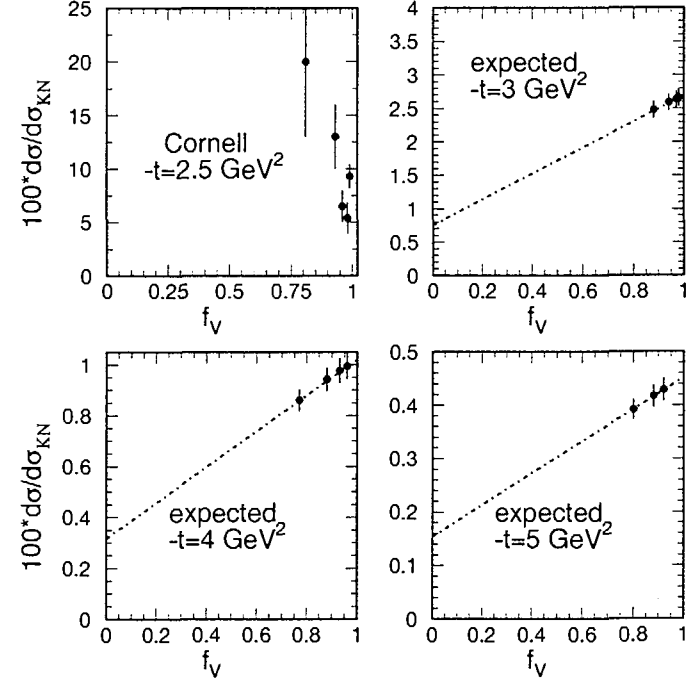


Figure 6: *A plot of the ratio $d\sigma/d\sigma_{KN}$, scaled by a factor of 100, as a function of $f_V$ at fixed $-t$. In the handbag model, the relationship is linear, with the limits $f_V = 1$ and 0 equal to $R_V^2$ and $R_A^2$, respectively. The upper left panel shows the Cornell data at $-t = 2.45$ GeV$^2$. The remaining panels show the expected precision at $-t = 3$-5 GeV$^2$ from the proposed experiment.*

10                                                                              11

nearly independent of the energy. For scattering from the proton, $A_{LL}$ will be diminished by the ratio $R_A/R_V$, but to the extent that these two functions track together with $t$, one expects $A_{LL}$ to be nearly independent of energy also. The handbag prediction at 4 GeV is shown in Fig. 7, along with pQCD predictions with various DA's [3]. The difference between the two mechanisms is remarkable. One of the goals of this proposal is to measure $A_{LL}$ at the fixed kinematics of 4 GeV, 110° ($-t=4$ GeV$^2$) in order to test the reaction mechanism and determine $R_A$ with an accuracy shown in Fig. 4.

The transverse polarization transfer observable $A_{LT}$ is defined by

$$A_{LT}\frac{d\sigma}{dt} \equiv \frac{d\sigma(\uparrow\rightarrow)}{dt} - \frac{d\sigma(\uparrow\leftarrow)}{dt} \tag{14}$$

where the first arrow refers to the incident photon helicity and the second to the recoil proton transverse polarization (normal to the proton motion and in the scattering plane). This observable arises as an interference between proton helicity flip and helicity non-flip amplitudes. In the strict pQCD limit, it must vanish since hadron helicity is conserved. Thus far this observable has not been calculated with either the pQCD or handbag mechanisms. However, one can anticipate that in the handbag mechanism, it will be proportional to $R_T$, the RCS form factor that is closely related to the Pauli elastic form factor $F_2$. Both are derived from the ND $\mathcal{K}^a(x;t)$, which is an object of intense current interest [20] since it is related to the contribution of quark orbital angular momentum to the proton spin. Indeed it was the original motivation [9] for the development of the concept of non-forward parton distributions. This interest was further stimulated by the recent results from experiment 93-027, a measurement of $G_{E_p}/G_{M_p}$, which shows that $Q^2F_2/F_1=1.3$ and is still rising at $Q^2=3.5$ GeV$^2$, contrary to the pQCD prediction that it saturates at 1. Another goal of the present proposal is to measure $A_{LT}$ at the one fixed point in order to learn additional information about the importance of helicity flip amplitudes in exclusive processes and perhaps measure the RCS form factor $R_T$.

The induced polarization $P_N$ is the component of recoil polarization normal to the scattering plane and involves the imaginary part of the interference between helicity flip and nonflip amplitudes. In the handbag mechanism, it is suppressed since all amplitudes are strictly real in this model [7]. In the strict pQCD limit, it vanishes due to hadron helicity conservation. No calculation has yet been done for this quantity.

Experimentally, one can in principle measure all three components of the proton polarization simultaneously using a focal plane polarimeter, as discussed in Sec. 3.8. Because of the spin precession in the spectrometer magnetic field, the longitudinal and normal components get mixed. We have chosen a kinematic point in which there is maximum sensitivity to the longitudinal polarization and therefore no sensitivity to the normal component, in order to optimize our well-defined test of the two reaction mechanisms for $A_{LL}$ (Fig. 7) and extract $R_A$. The measurement of $A_{LT}$ is not affected by the spin precession. We propose to measure both $A_{LL}$ and $A_{LT}$, each with a precision of ±0.1.

## 2.5  Goals of the Experiment

We propose measurements of cross sections in the energy range 3-6 GeV ($s=6.1$-$11.5$ GeV$^2$) and angular range $\theta_{cm}=60°$-$135°$ ($-t$ up to 6.5 GeV$^2$) (see Fig. 8), with an expected statistical precision of 5% and systematic uncertainty in the absolute cross sections of about 6%. Our specific goals are as follows.

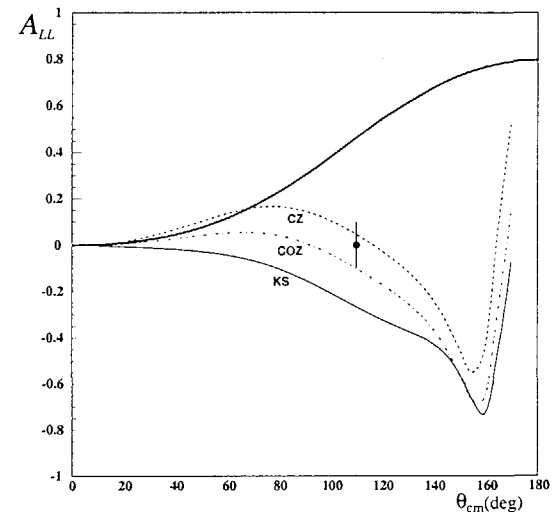1. Measure the scaling power $n(\theta)$ in the angular range $\theta_{cm} = 70° - 110°$ (see Fig. 3).



Figure 7: *Longitudinal polarization transfer parameter $A_{LL}$ at 4 GeV. The solid curve is the prediction based on the handbag mechanism with the form factors shown in Fig. 4. The other curves are pQCD calculations with various DA's. The point and error bar shows the projected precision from the present proposal.*

2. Test the approximate $s$-independence of the ratio $\sigma/\sigma_{KN}$ at fixed $t$ in the range $-t = 2.0$-$6.5$ GeV$^2$ and E= $3-6$ GeV (see Fig. 6).

3. Measure the form factor $R_V(t)$ in the range $-t = 2.0 - 6.5$ GeV$^2$, with precision ranging from about 2% on the low side to about 10% on the high side (see Fig. 4).

4. Test qualitative predictions for the longitudinal and transverse components of the recoil polarization at $-t = 4$ GeV$^2$ (see Fig. 7).

5. Determine the form factor $R_A$ at $-t = 4$ GeV$^2$ by measuring the polarization transfer observable $A_{LL}$ to a precision of ±0.1 (see Fig. 4).

6. Determine the form factor $R_T$ at $-t = 4$ GeV$^2$ by measuring the polarization transfer observable $A_{LT}$ to a precision of ±0.1.
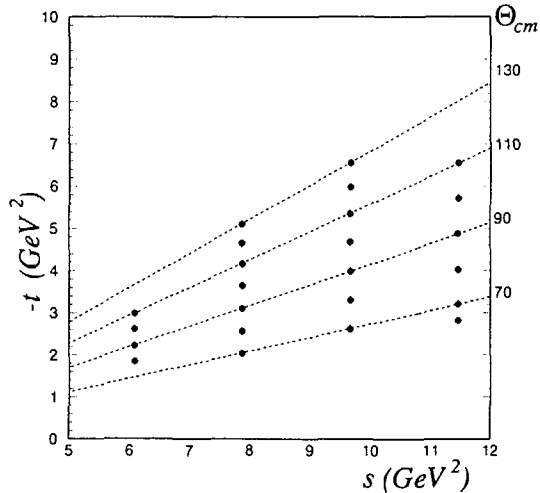
Figure 8: *Kinematics for E97-108. The dashed lines are contours of fixed $\theta_{cm}$.*



Figure 9: *Plan view of the proposed experiment in Hall A.*

## 3  Experimental Aspects

### 3.1  Overview

We propose to measure differential cross sections for Compton scattering from the proton $p(\gamma,\gamma'p)$ at incident photon energies between 3 and 6 GeV and over a wide range of CM scattering angles. In addition we propose a single measurement of the proton recoil polarization at 4 GeV using a polarized photon beam. Both sets of measurements utilize the technique shown schematically in Fig. 9. A high duty factor electron beam with current $\geq 10$ $\mu$A is incident on a 6% copper radiator located just upstream of the scattering target. The mixed beam of electrons and bremsstrahlung photons is incident on a 15-cm LH$_2$ target. For incident photons near the bremsstrahlung endpoint, the recoil proton and scattered photon are detected with high angular precision in a magnetic spectrometer and photon spectrometer, respectively. The magnetic spectrometer is one of the pair of High Resolution Spectrometers (HRS) that are part of the standard Hall A equipment, along with the cryogenic hydrogen target and bremsstrahlung radiator. The photon spectrometer is a new piece of equipment which is being constructed for this experiment. For the polarization measurements, a longitudinally polarized electron beam is used and the polarization is nearly completely transferred to the bremsstrahlung photon. The components of the polarization of the recoil proton are measured in the focal plane polarimeter (FPP) which is also part of the standard Hall A equipment.

One essential feature of the experimental technique is the use of the kinematic correlation
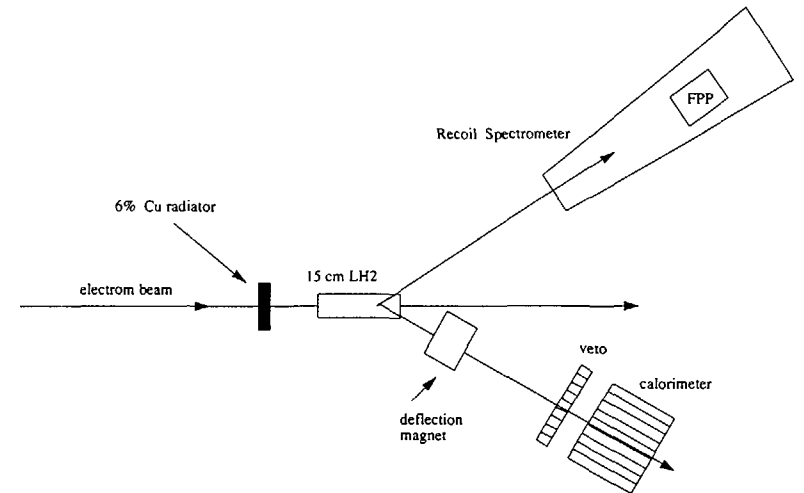
between the scattered photon and recoil proton in the RCS reaction to reduce the background of $\pi^0$ decay photons from the $p(\gamma,\pi^0 p)$ reaction, thereby placing stringent demands on the combined angular resolution of two-spectrometer system. A second essential feature is the mixed electron-photon beam, which is required in order to achieve the desired photon luminosity. On the one hand, this introduces the necessity to identify and reject electrons from $ep$ elastic scattering, while on the other hand it provides a convenient tool for an *in situ* calibration of the photon spectrometer and normalization of cross sections.

The principal new piece of equipment for this experiment is the photon spectrometer, which is described in more detail in Section 3.3. As a result of the feasibility experiments discussed in Section 3.2, the important components for the photon spectrometer have been identified and construction is under way. The principal component is a large-area segmented Pb-glass calorimeter with modest energy resolution and excellent position resolution. In order to reduce the potential background of electrons from $ep$ elastic scattering, which are kinematically indistinguishable from RCS photons, several techniques will be used. First, the number of $ep$ elastic electrons will be considerably reduced by avoiding the region very close to the bremsstrahlung endpoint, where the $e/\gamma$ ratio in the beam is very large. Next, electrons will be identified in a plexiglass Čerenkov veto detector that is segmented to allow for a veto that is spatially correlated with an event in the calorimeter. Finally, a magnet will be used to deflect the $ep$ elastic electrons by $\geq 10$ cm on the front face of the calorimeter, thereby allowing identification by altering the kinematic correlation

with the recoil proton relative to undeflected RCS photons. The mixed $\gamma - e$ beam is advantageous in that the $ep$ electrons can be used to calibrate the photon spectrometer. For this purpose, several planes of MWPC just in front of the calorimeter will be used in a separate *in situ ep* elastic scattering experiment to calibrate the position of each element of the calorimeter and veto detector, measure the position resolution, and measure the veto efficiency. The data acquisition electronics will utilize a variety of commercial NIM, CAMAC, and FASTBUS modules as well as some custom designed modules for the fast trigger. The entire spectrometer will be mounted on a mechanical assembly that allows changes in both scattering angle and radial distance, the latter needed to match the photon acceptance to that of the proton at different kinematic settings.

The kinematics we have chosen to investigate is shown in Fig. 8 as well as in Tables 1 and 2. Specifically, we propose 24 measurements that are arranged in order to study the $s$-dependence of the cross section at five center-of-mass scattering angles in the range 70°-110°; to study the behavior of the cross section at fixed $-t$ in the range 2-6 GeV$^2$; and to study the $t$-dependence of the cross section at the fixed $s$ corresponding to 4, 5, and 6 GeV beams. The angular limits of the 6 GeV measurements are dictated on the low end ($\theta_{cm} = 70°$) by the need to keep the photon detector at a laboratory angle no smaller than 20° due to the severe increase in background of low energy electrons and photons below that angle, and on the high side by the maximum momentum accessible with the HRS (4.5 GeV for the spectrometer normally used as the electron arm). For the recoil polarization transfer experiment, a single measurement at E=4 GeV, $\theta_{cm}$=90° (-$t$=3 GeV$^2$) is planned.

The technique we will use is conceptually identical to that used in the Cornell experiment. However, the combined effects of a high quality, high duty factor electron beam, a state-of-the-art magnetic spectrometer, the ability to calibrate *in situ* with *ep* elastic scattering, and high segmentation in the photon detector should allow significantly better measurements in the range of $s$ and $t$ already covered by Cornell, as well as significant extensions beyond that. The equipment would also be suitable for measurements at higher energies, should those energies become available at JLab in the future.

## 3.2 Results of Feasibility Studies

During 1998, a prototype photon spectrometer was built and tested with both parasitic and dedicated beam time at JLab. In effect, a small-scale model of the full detector was constructed and used in a real experiment. The principal components of the prototype were as follows: a calorimeter consisting of a 20x20 cm$^2$ array of lead glass blocks of type TF-1, each detector with dimensions 4x4x40 cm$^3$; two planes of veto hodoscope, one vertical and one horizontal, each composed of 4 cm wide x 10 cm long x 4 cm thick strips of plastic scintillator; and two planes of MWPC with 1 mm wire spacing. Most of the tests utilized a 4.1 GeV electron beam, with currents ranging from a few to 60 $\mu$A, with the photon detector at about 35° and 10 m from the target. The target options included a 15 cm and 4 cm LH$_2$ targets, the latter equipped with a 6% Cu radiator 26 cm from the target center. The photon electronics were fully incorporated into the Hall A data acquisition, allowing the detection of coincidences with the hadron HRS and full readout of both the photon spectrometer and HRS detector package. The only missing component in the setup was a suitable deflection magnet. The results of the tests are summarized as follows:

1. For scattering angles as small as 20°, the minimum anticipated, and at luminosities appropriate for the actual RCS experiment, the calorimeter operated in a stable manner with no significant deterioration of the energy or position resolution. Indeed, the measured counting rates and energy flows were generally about a factor of two below those predicted by a detailed Monte-Carlo

calculation. Therefore the desired luminosities can be achieved with no loss of performance of the calorimeter. Moreover, the measurements show *no noticeable degradation* (i.e., $\leq$ 2%) in the pulse height of the calorimeter blocks after a radiation dose approximately half that expected for the entire RCS experiment, thereby obviating the need to use radiation hardened lead glass.

2. A position resolution $\sigma_x \approx 5.4$ mm and an energy resolution $\sigma_E/E \approx 4.6\%$ (see Fig. 10)were achieved for $\approx$ 2.2 GeV electrons, both of which are sufficient for the experiment. The position resolution contributed only 0.6 mr to the overall angular resolution, which was measured to be about 2.8 and 3.2 mr for the in-plane and out-of-plane angles, respectively (see Fig. 11) and was dominated by the hadron arm. Although adequate for the RCS experiment (see Section 3.4), improved HRS angular resolution is desirable. Coincidences between the HRS and calorimeter provide an excellent technique to measure and optimize the HRS angular resolution, and an attempt will be made to do so in the near future.

3. The MWPC works as a calibration device for currents up to 5 $\mu$A. It was used to measure the position resolution of the calorimeter. A new prototype chamber has been built and will be tested during summer 1999, with the goal of using it as part of the veto detector during the RCS experiment itself rather than just as a calibration detector.

4. It was determined that segmentation of the veto detector is essential in view of the large counting rates. The initial choice of 4-cm thick plastic scintillators has been successful. Despite the high counting rates, the veto provided efficient discrimination against electrons. However, it is likely that a plexiglass Čerenkov detector will be even more effective in view of its reduced sensitivity to low velocity particles, and tests of these detectors under realistic beam conditions are in progress.

5. At luminosities needed for RCS, the raw coincidence spectrum between the calorimeter and HRS is very clean (see Fig. 12) under realistic running conditions for the kinematics $s \approx 8$ and $-t \approx 3$ GeV$^2$. Moreover, it is clear that this can be improved further both by appropriate cuts in the proton and photon kinematics and by matching the timing of each Pb-glass block. We conclude that chance coincidences will not be a problem for the RCS experiment.

6. As a "proof of principle", the actual RCS experiment was performed, the results of which are summarized in Figs. 13 and 14. The conclusions are that the $\pi^0$ background is understood and under control; that the mixed photon-electron beam can be dealt with and is actually a desirable feature in that it allows *in situ* calibrations; that the background in the hadron HRS when working at photon energies below the bremsstrahlung endpoint are manageable; and that the experiment is feasible with the planned equipment.

## 3.3 Photon Spectrometer

The key new piece of instrumentation is the photon calorimeter, which will consist of 702 lead-glass blocks of type TF-1, the identical blocks that have performed so well during the feasibility experiment. As already remarked, the feasibility studies have shown that radiation hardened lead glass is not necessary for the RCS experiment. The array of blocks, each with dimensions 4x4x40 cm$^3$ and with an expected position resolution of order 5 mm, will be arranged into an rectangular array of 26 columns by 27 rows (approximately 1m x 1m). All lead glass and PMT's will be provided by the Yerevan collaborators. A total of 200 blocks and PMT's are already at Jlab and the remainder will be delivered during 1999. A design for packaging the blocks into a working calorimeter, including design of the PMT bases, is complete and construction is in progress.

It is desirable to match the angular acceptance of the calorimeter to that of the proton arm. In
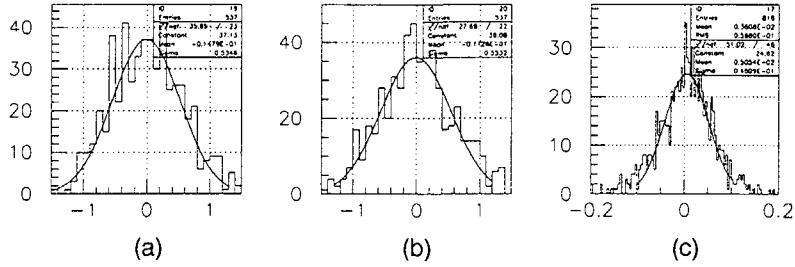
Figure 10: *Position resolution in the (a) x and (b) y coordinates and (c) energy resolution achieved during the feasibility studies. The position plots show the difference in cm of the electron position measured in the calorimeter and that expected from the hit pattern in the MWPC. The overall position resolution is about 5.4 mm in each coordinate. The energy plot shows the fractional difference between the energy measured in the calorimeter and that expected based on the recoil proton kinematics. The energy resolution achieved is 4.6% at 2.2 GeV.*
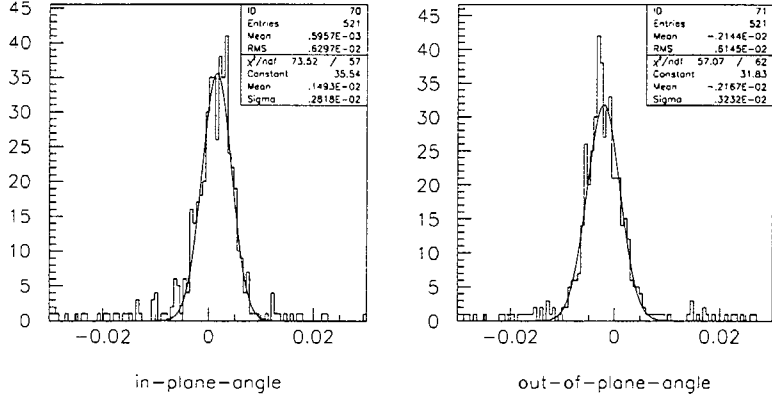


Figure 11: *Angular resolution of the combined HRS-calorimeter system for in-plane (left) and out-of-plane angles (right). Plotted is the difference in mr between the electron angle measured in the calorimeter and that expected based on the recoil proton kinematics. The overall angular resolution is 2.8 mr and 3.2 mr for the in-plane and out-of-plane angles, respectively.*
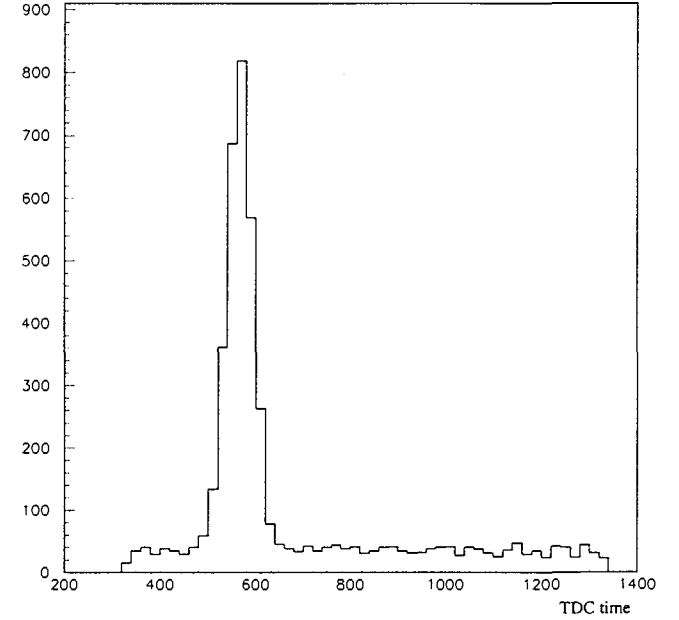


Figure 12: *TDC spectrum for coincidences between the calorimeter and the HRS for the run with a 6% radiator, the 4 cm LH₂ target, the off-endpoint kinematics, and a beam current of 10 μA.*

the vertical plane, the acceptance required is

$$\Delta\phi_\gamma = \frac{\sin\theta_\gamma}{\sin\theta_p}\,\Delta\theta_p = \pm\frac{\sin\theta_\gamma}{\sin\theta_p}\,[25\text{mr}] \qquad (15)$$

This relation follows from the coplanarity condition on the proton and photon. Since large photon angles $\theta_\gamma$ are correlated with small recoil proton angles, the required vertical acceptance $\Delta\phi_\gamma$ grows very large at large angles. The horizontal acceptance is more complicated, since it depends on both the angular $\Delta\theta_p$ and momentum $\Delta p_p$ acceptance of the proton spectrometer, as well as on the limitations imposed by $\Delta E_\gamma/E_\gamma$, which will be kept under 10%. We have calculated the necessary acceptance in both $\phi_\gamma$ and $\theta_\gamma$ for all the kinematics of the experiment. The results for the 5 GeV kinematics (for which the angular range is greatest) are shown in Fig. 15. We see that the required $\Delta\theta_\gamma$ also grows large at large scattering angles, although not as rapidly as the required $\Delta\phi_\gamma$. Our detector will have an angular acceptance that can be adjusted at each scattering angle to match the horizontal angular acceptance (see Table 1). The movement will be achieved by mounting the

Figure 13: *Energy and angular plots for coincidence events with the 6% radiator and 4 cm LH₂ target. The top row includes all the selected coincidence events, whereas the middle and bottom rows are those selected events satisfying the elect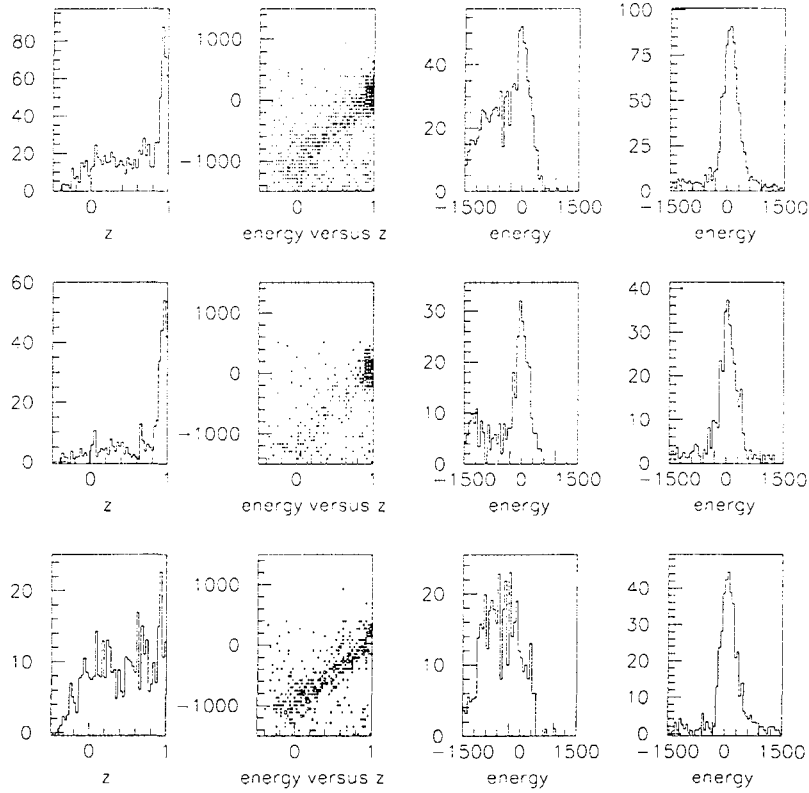ron and photon cuts, respectively, in the veto detector. For each row, the first column is the parameter z, which is the cosine of the $\pi^0$ decay angle in its rest frame relative to the $\pi^0$ direction in the Lab and is reconstructed from the proton kinematics and photon angle measured in the calorimeter. The third column is the difference between the measured photon energy and that reconstructed based on ep kinematics. The second column is a scatter plot of the energy difference and z. The fourth column is the difference between the measured photon energy and that reconstructed based on $(\gamma, \pi^0)$ kinematics (using the z information). In the z distribution, the peak near z = 1 comes from events having two-body kinematics, primarily ep scattering and RCS.*



Figure 14: *Proof of principle experiment for RCS at 4 GeV and $\theta_{cm} = 90°$. All panels show the difference between the measured out-of-plane angle φ in the calorimeter and the reconstructed angle based on the HRS measurement and two-body kinematics. The upper left panel shows all coincidence events. The peak at φ = 0 is due primarily to ep scattering and secondarily to RCS, whereas the continuum is due to $\pi^0$ decay photons. For the middle left panel, a cut is made requiring that the in-plane angle θ be close to that expected for two-body kinematics; this clearly enhances the central peak. The lower left panel in addition demands a signal in the veto detector, thereby selective picking out the ep events. The right panels demand no signal in the veto, thereby picking out photons. An anti-cut on the in-plane angle (middle right) preferentially picks out $\pi^0$ decay photons, whereas a cut on the in-plane angle (bottom right) selectively enhances the RCS events, with some continuum mixed in. Therefore, the events above the dashed line in the lower right panel represent RCS events, with a 10% contamination due to the inefficiency of the veto detector. The number of RCS events agree within statistics with the Cornell measurements.*

detector on a platform that allows both rotation about the target position and radial movement, as discussed below
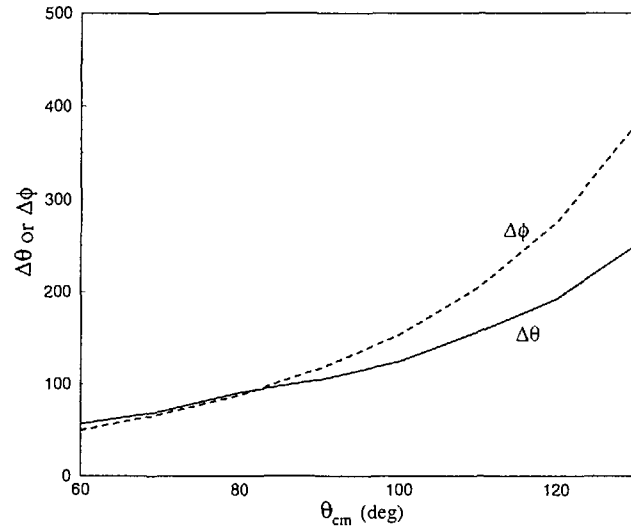


Figure 15: *The angular acceptance of the photon spectrometer needed to match the acceptance in the proton arm as a function of $\theta_{cm}$ at E=5 GeV.*

Since we will primarily use angular kinematics to identify Compton events, only modest energy resolution is needed. The BNL group [21] reports an energy resolution

$$\sigma_E = .06\sqrt{E} + .02E, \tag{16}$$

which should suffice for our purposes.

In order to identify electrons from $ep$ scattering, two planes of veto detectors (vertical and horizontal) will be constructed. The feasibility studies have shown that the counting rates in the veto will be large, so that it is necessary to segment the detectors to keep the rate in any given detector less than about 500 kHz. The segmentation also allows for spatial correlations between the veto and calorimeter. Multi-hit TDC's will be used to improve the veto efficiency at high counting rates. Although the total rate in each plane of veto counters will be high, demanding a spatially correlated coincidence between the two planes reduces the chance veto probability to a negligible level. In the present design, each plane consists of two rows of solid ultra-violet transmitting (UVT) plexiglass (acrylic) radiators, each viewed by one photomultiplier tube (PMT). Current plans call for each detector be rectangular in cross section and cover a 2 cm x 50 cm area, with a thickness

of 4 cm, for a total of 100 detectors for each plane. Feasibility tests of this arrangement are in progress.

In order to provide a redundancy in the identification of $ep$ elastic electrons, a deflection magnet will be placed between the target and the calorimeter, as close as possible to the target. A field integral of 0.25 T-m is sufficient to deflect electrons at least 10 cm at the front face of the calorimeter, which is considerably larger than the expected position resolution of the calorimeter. The field integral needs to be uniform to a few percent. A preliminary design for such a magnet exists, at the modest cost of $35k. This is considerably less expensive than shipping to JLab an existing magnet from another facility, although that option has not been ruled out. An appropriate power supply and associated infrastructure already exists at JLab.

The feasibility experiment has already demonstrated that the MWPC is extremely useful as a calibration detector for the rest of the photon spectrometer. For calibrations, which use $ep$ scattering from the main electron beam (without a radiator), low luminosities can be used and issues of counting rate are not important. For this purpose, two planes of MWPC would suffice (X,Y). It is not yet clear whether a wire chamber can be constructed that will operate at the much higher lumonisities needed for the RCS experiment. If so, then the MWPC serves as an additional very effective veto detector because of the high degree of spatial correlation with the calorimeter. For this purpose, three planes of MWPC (X,Y,U) would be needed to resolve track ambiguities and increase the veto efficiency. It is also quite likely the readout electronics would need to be more elaborate for this latter option since the overall counting rate would be much larger. For either option, the wire-chamber package will have active-area dimensions of 1 m x 1 m. The wire planes are standard MWPC with several large-diameter guard wires at the extreme edges of each wire plane to reduce edge effects and suppress discharge at the boundaries. The X and Y planes will have wire spacings of 3 mm. A common cathode is located between these two planes. The U plane spacing will be 4.07 mm. All wires will have diameter 25 $\mu$m. The cathode-to-anode spacing will be 6.35 mm, and the cathode foils will be double-sided gold-plated mylar. These dimensions are copied from successful chambers built by IUCF recently. An Ar-$CO_2$ gas mixture (80/20) is planned. In-beam testing of a prototype chamber with 2 mm wire spacing is planned for summer 1999.

The data acquisition utilizes the standard Hall A trigger supervisor, the standard HRS readout package, and a separate readout package which is being developed for the photon spectrometer. The current plan is to perform all the coincidence triggering locally at the calorimeter electronics. A fast trigger signal from the HRS focal plane would be used to gate the photon-arm ADC's and TDC's and to check for coincidences with the calorimeter trigger. A fast-clear operation will be performed in the absence of a coincidence event. This avoids long and costly cable delays and keeps the rate of fast-clears at a low level determined by the rate of hadron triggers. The calorimeter trigger will be formed with a custom-designed linear fan-in module that ultimately combines analog signals from overlapping 16 x 2 subarrays of blocks into a signal which goes to a discriminator. A total of 48 such discriminators are logically OR'd to obtain a calorimeter trigger. For the calorimeter, 702 channels of Fastbus ADC's are needed. Each of the 200 veto detectors requires a discrimininator/fan-out, a Fastbus ADC, and a Fastbus TDC, the latter being multihit to assure good veto efficiency at high counting rates. Up to 1000 channels of either latch or TDC will be needed for the MWPC, with the choice awaiting the completion of the prototyping. The expected trigger rates in this experiment will be high and will place great demands on the data acquisition system. Issues such as the limitations on the fast-clear and data acquisition rates, suitability of particular choices for ADC's and TDC's, and synchronization of the data stream at high rates are currently under study.

Based on the feasibility measurements, we expect calorimeter trigger rates to be less than about 1 Mhz. With a coincidence resolving time of 10 ns, this implies less than 1% accidental coincidences. If necessary, this can be further reduced by taking advantage of the spatial correlation between the recoil proton and scattered photon and having a TDC for each 16 x 2 subarray.

The detector platform needs to be designed to allow changes of scattering angle as well as radial distance to the target. Since the position of the detector will be calibrated at each kinematic setting, the alignment requirements can be relaxed considerably. We are presently considering a standalone assembly consisting of a large stand that is positioned in Hall A with air pads. The detector will be surveyed relative to alignment fiducials on the base of the stand, which will then be positioned with respect to fixed marks on the floor of the hall.

## 3.4 Background from $\pi^0$ Photons

The goal is to separate the $p(\gamma, \gamma'p)$ events from the $p(\gamma, \pi^0 p)$ events. Because of the small mass of the pion, the four-momentum of a coherently produced $\pi^0$ is nearly identical to that of a Compton photon. For a monochromatic incident photon beam, it would be possible to resolve Compton from $\pi^0$ events by a precise measurement of the three-momentum of the recoil proton (indeed, this is essentially the technique used in the VCS experiments), but this will not work for a continuous bremsstrahlung spectrum. Instead one relies on the kinematic correlation between the recoil proton and the associated Compton photon or $\pi^0$. Under the assumption of two-body kinematics, a measurement of the three-momentum of the recoil proton uniquely defines both the energy of the photon that initiated the event and the three-momentum of the photon or $\pi^0$. The $\pi^0$ decays into two photons. The higher energy photon has an energy between $E_\pi/2$ and $E_\pi \approx E'_\gamma$ (the energy of a scattered photon in the same kinematics) and is confined to a cone of half-angle $m_\pi/E_\pi$ about the pion direction. The lower energy photon has an energy less than $E_\pi/2$ and lies outside the cone. In contrast, for fixed kinematics of the recoil, the Compton photon is spread out in solid angle only by the overall angular resolution of the coincidence detection system. This resolution is determined by the intrinsic resolution of the magnetic spectrometer for the in-plane and out-of-plane proton angles and for vertex reconstruction; by proton multiple scattering in the target and other material; by the angular spread of the incident photon beam; and by and the ability of the calorimeter to determine the angle of the scattered photon. We combine all these effects into effective Compton angular resolutions, which we denote by $\sigma_\theta$ and $\sigma_\phi$ for the horizontal and vertical directions, respectively. The ratio $R_{\pi^0}$ of coherent $\pi^0$ photons to Compton photons is therefore determined by the ratio of cross sections divided by the fraction of the $\pi^0$ photons falling within the angular resolution. One easily finds

$$R_{\pi^0} = 11 \frac{d\sigma(\gamma, \pi^0)}{d\sigma(\gamma, \gamma)} \frac{\sigma_\theta \sigma_\phi}{(m_\pi/E'_\gamma)^2}, \tag{17}$$

where the numerical factor comes in part from the fraction of Compton events within $2\sigma$ of a two-dimensional Gaussian distribution.

We see then that the Compton and $\pi^0$ events are distinguished by the distributions of $\delta\theta_\gamma$ and $\delta\phi_\gamma$ which are, respectively, the difference between the measured photon angles and those photon angles reconstructed based on the measurement of the proton kinematics. Typical distributions of these quantities measured in the feasibility experiment are shown in Fig. 11. The resolutions in these quantities, $\sigma_\theta$ and $\sigma_\phi$, respectively, directly enter into the expression for $R_{\pi^0}$ given above. It is important to note that enough of the $\pi^0$ photon distribution can be measured in the experiment to interpolate the distribution accurately under the Compton peak. Therefore, the running time

needed to obtain a given statistical precision in the measurement of the Compton cross section is proportional to $1+R_{\pi^0}$.

As an example, we present a detailed estimate of $\sigma_\phi$ and $\sigma_\theta$ for the specific case of 6 GeV at 110°. The quantity $\sigma_\phi$ has contributions from the following:

- $\sigma_x^\gamma$, the position resolution of the calorimeter. We assume this to be 5 mm, as discussed earlier. At a distance of 6 m (determined by the horizontal angular acceptance), this contributes 0.8 mr to $\sigma_\phi$.

- $\sigma_\phi^p$, the out-of-plane angular resolution of the HRS, which we take to be 0.9 mr, a value that has already been achieved. This leads to a contribution to $\sigma_\phi$ of 1.8 mr.

- The proton multiple scattering in the target. This is calculated using standard formulas, taking into account the hydrogen in the target, the aluminum wall of the target can, and the exit aluminum foil to the scattering chamber. Together these contribute 0.8 mr.

- The vertical angular spread of the photon beam. This is calculated assuming it is due to multiple scattering by the electron beam in the radiator. It contributes 1.0 mr.

- The vertical beam spot size. We calculate this by assuming the spot size is due to the angular spread and therefore less than 1 mm. It contributes 0.8 mr.

Similarly, $\sigma_\theta$ has contributions from the following:

- $\sigma_x^\gamma$, the position resolution of the calorimeter. Once again, this contributes 0.8 mr.

- $\sigma_\theta^p$, the in-plane angular resolution of the HRS, which we take to be 0.9 mr, a value that has already been achieved. This leads to a contribution of 3.3 mr.

- the proton multiple scattering in the target. This contributes 1.4 mr.

- The horizontal angular spread of the photon beam. This contributes 1.0 mr.

- The horizontal beam spot size. This contributes 0.1 mr.

- $\sigma_y^p$, the resolution in proton vertex reconstruction transverse to the spectrometer axis. We use the value 0.7 mm that has been achieved, leading to a contribution of 0.3 mr.

- $\sigma_p$, the proton momentum resolution. This contributes negligibly.

Combining these independent contributions in quadrature, we find $\sigma_\theta$=3.8 mr and $\sigma_\phi$=2.5 mr. By comparison, the Cornell experiment achieved 8.5 in $\theta$ and 2.1 in $\phi$. The above number show that these results are dominated by contributions from the HRS, $\sigma_\theta^p$ and $\sigma_\phi^p$, so that is where any improvements should be aimed. The resolutions calculated for all our proposed kinematics are given in Table 2.

To calculate $R_{\pi^0}$, we use the expression of Eq. 7 for the RCS cross section, with form factors from Fig. 4. For the $p(\gamma, \pi^0 p)$ cross section, we assume

$$\frac{d\sigma(\gamma, \pi^0)}{dt} = 40 \frac{8.4 \, GeV^2}{s} \frac{d\sigma(\gamma, \gamma)}{dt}, \tag{18}$$

where the numerical factor comes from the Cornell data and the $s$-dependence is that expected from asymptotic scaling. In Table 2, we see that $R_{\pi^0} \approx 0.6$, essentially independent of our kinematics. The worse angular resolution at backward angles (as the detector moves closer to the target) is compensated by the larger $\pi^0$ cone.

## 3.5 Background from e-p Scattering

As discussed above, the presence of electrons in the beam introduces backgrounds that are kinematically indistinguishable from Compton scattering. The first is simply elastic $ep$ scattering, where the scattered electron is detected in the calorimeter. The second is $ep$ scattering followed by emission of a hard bremsstrahlung photon in the direction of the scattered electron, which we refer to as an $ep\gamma$ event. As remarked earlier, since most of the electrons in the beam are at the bremsstrahlung endpoint, we eliminate much of the problem by tuning the spectrometer to accept events corresponding to incident photons in the range $E_\gamma^{min}$ to $E_\gamma^{max}$, where $E_\gamma^{max}$ is approximately 0.1 GeV from the endpoint. We further assume $E_\gamma^{max}/E_\gamma^{min} \approx 1.1$. It is now straightforward to estimate the scope of the problem. To do this, we use the Matthews and Owens bremsstrahlung spectrum [22] to count the relative numbers of bremsstrahlung photons and post-bremsstrahlung electrons in the interval between $E_\gamma^{min}$ and $E_\gamma^{max}$. We use the Rosenbluth cross section for $ep$ scattering and Eq. 7 for the Compton cross section, with the form factors from Fig. 4. The calculated ratio of scattered electrons to photon $N_{ep}/N_{\gamma p}$ for the proposed kinematics is given in Table 2. It ranges from a few at the backward angles to ten's at the forward angles. In the worst case, we need to reject $ep$ elastic events at the level of about 1 part in 1000 in order to keep the $ep$ background at a reasonable level, and this will be done with the techniques discussed above in Section 3.3.

We now estimate the $ep\gamma$ problem by calculating the probability that the scattered electron will radiate a photon in the energy range $E_\gamma^{min}$ to $E_\gamma^{max}$, including both the external and internal bremsstrahlung. Using a Monte Carlo calculation and including the effects of detector resolution, we find that at 6 GeV the ratio of $ep\gamma$ to Compton events is approximately 20% at 70°, 10% at 90° and 6% at 110° (see Table 2). Sample histograms for the 6 GeV 70° and 110° points are shown in Fig. 16 and 17, respectively. We remark that this is one case where it would be beneficial to have good energy resolution in the calorimeter, since the bremsstrahlung background steeply rises at low energy, whereas the Compton photons are concentrated at high energy. The shape of the background can easily measured through the calibration procedure described in Sec. 3.9.

## 3.6 Other Backgrounds

Within one pion mass from the bremsstrahlung endpoint, only elastic scattering and $\pi^0$ photo-production are possible. However, in the present experiment, we will use incident photons as much as 0.7 GeV below the endpoint (in the case of a 6 GeV beam). However, any $\geq$ 3-body final state will not have a strong kinematic correlation between the recoil proton and the detected photon. For example, consider the case of $\eta$ photoproduction followed by decay to two photons. The kinematics for this process is similar to the $\pi^0$ case except that the $\eta$ is four times more massive, so that the decay cone is 16 times wider. This would give rise to a smooth background under the $\pi^0$ cone, which includes the Compton events, so that the good angular resolution discriminates against such background. Another example is inelastic photon scattering leaving the proton in an excited state, which then decays into a proton and pion. Once again, the smearing of the kinematics due to the momentum of the third particle (in this case, the pion) gives rise to a cone roughly centered on the Compton kinematics. For the specific case of scattering into the $\Delta$ resonance, the decay cone is about 50% larger than the $\pi^0$ cone. In investigating whether such a background exists, it is useful to have sufficient angular acceptance to look outside the $\pi^0$ cone for the presence of a smooth background that can be extrapolated into the region of interest and subtracted. This procedure was followed in the Cornell experiment, where very little background was found [11]. We will follow a similar procedure in the proposed measurements.

Figure 16: *Monte Carlo calculation of the energy spectrum of RCS plus $ep\gamma$ photons (solid) and $ep\gamma$ photons alone (dashed) for E=6 GeV, $\theta_{cm}$=70°. It has been assumed that backgrounds from ep elastic scattering and $\pi^0$ photons have been removed by appropriate kinematic cuts. The ratio of $ep\gamma$ to RCS events in the region above 3500 MeV is $\approx$ 0.20.*
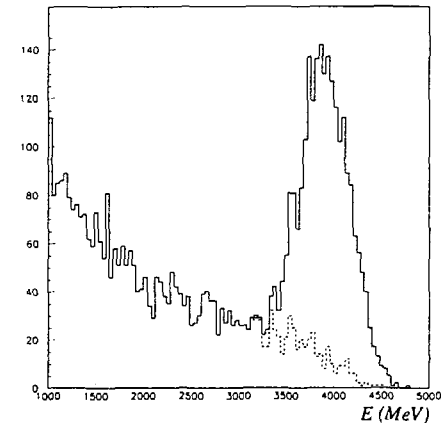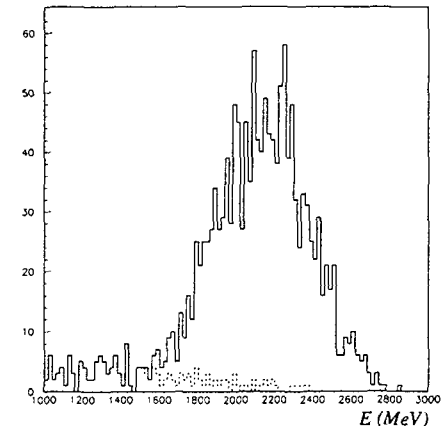


Figure 17: *Monte Carlo calculation of the energy spectrum of RCS plus $ep\gamma$ photons (solid) and $ep\gamma$ photons alone (dashed) for E=6 GeV, $\theta_{cm}$=110°. It has been assumed that backgrounds from ep elastic scattering and $\pi^0$ photons have been removed by appropriate kinematic cuts. The ratio of $ep\gamma$ to RCS events in the region above 1500 MeV is $\approx$ 0.06.*

## 3.7 Luminosity Considerations

We now address the issue of luminosity limitations imposed by the counting rates in the photon arm. Our approach has been to do measurements in some limited kinematic range and then use a Monte Carlo code to extrapolate into other regions. The code we have used was designed for radiation shielding calculations and uses the DINREG event generator in the framework of GEANT detector simulations and particle transport code. The measurements were discussed in Section 3.2. At 4 GeV and 35°, the measured counting rates and energy flows were comparable, although less than, those predicted by the code.

With the Monte Carlo code reasonably calibrated, we now use it to extrapolate to kinematics and luminosities of interest to the Compton experiment, for which we will use a copper radiator of thickness 0.8 g/cm² (6% radiation length), a scattering target of 1 g/cm² Hydrogen, and a beam of intensity 10 $\mu$A. The worst case situation is the 6 GeV point at $\theta_{cm} = 65°$, for which the calorimeter is at $\theta_{lab} \sim 20°$ and the scattered photons/electrons have an energy of 4.3 GeV. Assuming a 1 m² detector at 17 m, the code predicts a total rate (electrons plus photons) of 4 MHz above 0.5 GeV and 0.5 MHz above 2 GeV. Given the high segmentation of the calorimeter and veto detectors, this should be a tolerable rate.

## 3.8 Counting Rate Estimates

The RCS event rate is given by

$$\frac{dN_{\gamma\gamma}}{dt} = TX\left[\frac{I}{e}\right]\frac{d\sigma}{d\Omega_p}\frac{\Delta E_\gamma \Delta\Omega_p}{E_\gamma}, \tag{19}$$

where $T$ is the target thickness, $X$ is the radiator thickness, $I$ is the beam current, $-e$ is the electron charge, $\bar{E}_\gamma$ is the mean incident photon energy over the acceptance interval $\Delta E_\gamma$, and $\Delta\Omega_p$ is the angular acceptance of the proton spectrometer. Rate estimates in counts/hour are given in Table 2. These estimates assume a 15-cm long liquid Hydrogen target ($T = 6.3 \times 10^{23}\, cm^{-2}$), a 6% radiator ($X = 0.06$), a modest beam current of 10 $\mu$A, and the standard HRS acceptances (51 mr and 102 mr for for the horizontal and vertical angles, $\pm4.5\%$ in momentum, and $\pm3$ cm in $y$). The calculation of the rates takes into account the geometrical acceptance of the calorimeter and uses the RCS cross section of Eq. 7 and Fig. 4. Also shown in Table 2 are the expected backgrounds due to the $\pi^0$ photons, $ep$, and $ep\gamma$.

For the polarization transfer measurement at E=4 GeV, $\theta_{cm}$=110°, the recoil proton momentum is 3.0 GeV/c. A longitudinally polarized photon beam is required. We assume polarization transferred to the bremsstrahlung photon according to the formula [23]

$$\frac{P_\gamma}{P_e} = \frac{y(4-y)}{4-4y+3y^2}, \tag{20}$$

where $y = E_\gamma/E = 0.93$ for the proposed measurement. Therefore we can expect $P_\gamma$ to be about 99% of $P_e$. We assume an electron polarization of 70%, which is currently being achieved in the Happex experiment. We further assume the same FPP characteristics as that assumed for E99-007, with the analyzer upgraded to 70 cm of polyethylene, which implies a figure of merit $\epsilon A_y^2 \approx 0.01$ at 3.0 GeV/c. Using the standard formula for the uncertainty in the measured polarization $\sigma_P$

$$\sigma_P = \frac{\pi}{2A_y P_\gamma \sqrt{N_\epsilon}}, \tag{21}$$

where $N$ is the number of events, we will need $N$=50,000 events to achieve a precision of $\sigma_P$=0.1. At this recoil momentum, the spin precession is 270° so that the measurement will have maximum sensitivity to the longitudinal component of the recoil polarization at the target and no sensitivity to the normal component. Referring to the counting rates in Table 2, and taking into account the $\pi^0$ background, it will therefore require 173 hours of beam to determine both $A_{LL}$ and $A_{LT}$ with a precision of 0.1. Using Eq. 11 and Diehl's model for $R_V$, this will determine $R_A$ to an absolute precision of $\pm0.01$.

It would be desirable to extend the polarization measurements to higher energy. Since both the cross sections and the FPP figure of merit fall as the energy goes up, the measurements become very time consuming. For example, to achieve a precision of 0.1 in the transverse polarization at E=5 GeV, $-t$=5 requires approximately 600 hours of beam while E=5 GeV, $-t$=6 requires over 1200 hours. For such measurements, it might be preferable to use a polarized target rather than detect the recoil polarization, in which case it would be necessary to develop techniques that would allow a clean photon beam on the target.

## 3.9 Calibrations and Systematic Errors

Our goal is to measure the Compton scattering cross section to a statistical precision of 5% and with overall systematic uncertainty on the order of 6%. In this section, we outline one possible calibration procedure, with particular attention to techniques to reduce the systematic errors.

Our plan is to measure the RCS cross section relative to the $ep$ elastic cross section, which is experimentally measured to better than 3.5% [24]. For each kinematic point, we do measurements with the deflection magnet both on (MON) and off (MOFF). Since the kinematics of RCS and $ep$ elastic are essentially identical, the same cuts on the HRS spectrometer can be used to select RCS events only (MON) or RCS plus $ep$ events (MOFF), or just $ep$ for MOFF events accompanied by a veto signal. Designating R as the measured ratio of RCS to $ep$ events, we have

$$\left(\frac{d\sigma}{dt}\right)_{RCS} = R\frac{N_\gamma}{N_e}\left(\frac{d\sigma}{dt}\right)_{ep}, \tag{22}$$

where $N_\gamma$ and $N_e$ are the number of incident photons and electrons, respectively, after passing through the 6% radiator. This technique of normalization is very appealing since it is independent of the acceptances of both the calorimeter and the HRS. Moreover it is insensitive to all effects associated with electron beam monitoring, target thickness, and data acquisition deadtime, as long as these effects are the same for the MON and MOFF runs. The cost of using this technique is that supplemental measurements must be done to determine $N_e$, the post-radiator energy spectrum of electrons. We propose measuring this with $ep$ elastic scattering using the pair of HRS spectrometers. By doing this measurement with and without a radiator, one can measure the number of energy-degraded post-radiator electrons per incident electron in the energy region of interest near the bremsstrahlung endpoint, with an accuracy of about 3.5%. We plan to do this measurement at two of the four energies in order to check and calibrate our calculation of $N_e$, which will be used at the other two energies.

Additional calibrations will be done once for each of the four beam energies at the most forward calorimeter angle:

1. Calibrations of the energy and position response of the calorimeter using $ep$ elastic scattering without a radiator and with the deflection magnet turned off. These measurements also utilize the MWPC for a precise position measurement.

2. Measurement of the shape and magnitude of the $ep\gamma$ spectrum using $ep$ elastic scattering without a radiator and with the deflection magnet turned on.

Finally, we plan runs at several kinematic points to check the background with the radiator removed and/or with an empty target.

We aim for an overall systematic uncertainty of about 6%. We arrive at this number from the sum in quadrature of three nearly identical contributions of 3.5% each: the $ep$ elastic cross section used for normalization; the post-radiator electron energy spectrum $N_e$; and the bremsstrahlung spectrum $N_\gamma$, the latter based on experience using mixed photon/electron beams in Hall C (E89-012) or at SLAC (NE17). We are exploring ways to test our calculation of $N_\gamma$ using the Hall B photon facility.

## 4 Beam Request

A summary of our beam request is given in Table 3. For the unpolarized measurements, the time needed to achieve 5% statistics for the RCS cross section, including the effect of the (modest) $\pi^0$ background, totals about 65 hours (see last column of Table 2). This represents about 1/3 of the total running time needed for this part of the experiment. The remainder of the time will be needed for calibrations with the electron beam as discussed in Sec. 3.9. Specifically, we budget the 128 hours of calibration time as follows:

1. 32 hours for $ep$ normalization measurements with magnet off (2% statistics)

2. 24 hours for measurement of the post-radiator electron spectrum $N_e$

3. 20 hours for energy and position calibrations of calorimeter

4. 32 hours for measurement of the $ep\gamma$ background spectrum

5. 20 hours for background checks with radiator removed and/or empty target

In addition we budget 4 hours for each of 3 energy changes and 2 hours for each of 20 angle changes (the latter requiring access into the hall to move and align the calorimeter by hand) for a total of 52 additional hours. Therefore, our beam request for the unpolarized cross sections is 245 hours. This request is essentially identical to that requested and approved by PAC13 for E97-108. For the polarization transfer measurement, we require an additional 173 hours of data taking and an additional 20 hours for setup and calibrations (including beam polarization measurements), arriving at 193 hours. Therefore, the total request in the is proposal is 438 hours (or 18.3 days).

## References

[1] A. S. Kronfeld and B. Nizic, Phys. Rev. **D44** (1991) 3445.

[2] G. R. Farrar and H. Zhang, Phys. Rev. Lett. **65** (1990) 1721;
Glennys R. Farrar and H. Zhang, Phys. Rev. **D41** (1990) 3348; and
E. Maina and G. R. Farrar, Phys. Lett. **B206** (1988) 120.

[3] M. Vanderhaeghen, *et al.*, Nucl. Phys. **A622** (1997) 144c.

[4] P. Kroll, M. Schürmann and W. Schweiger, Nucl. Phys. Int. J. Mod. Phys. **A6** (1991) 4107.

[5] P. Kroll, M. Schürmann, and P. A. M. Guichon, Nucl. Phys. **A598**(1996) 435 .

[6] A. Radyushkin, Phys. Rev. D **58** (1998) 114008.

[7] M. Diehl, Th. Feldman, R. Jakob, and P. Kroll, hep-ph/9811253, hep-ph/9903268.

[8] J. Bolz and P. Kroll, Z. Phys. **A356**(1996) 327

[9] X. Ji, Phys. Rev. Lett. **78** (1997) 610; Phys. Rev. D **55** (1997) 7114.

[10] A. Radyushkin, Phys. Rev. D **56** (1997) 5524.

[11] M.A. Shupe *et al.*, Phys. Rev. **D19** (1979) 1929.

[12] S.J. Brodsky and G. Farrar, Phys. Rev. Lett. **31** (1973) 1953.

[13] R.P. Feynman, **Photon-Hadron Interaction**, W.A. Benjamin, Reading MA, 1972.

[14] P.A.M.Guichon and M. Vanderhaeghen, Progress in Nuclear Physics **41** (1998) 125.

[15] A.V. Radyushkin, Phys. Lett. **B380** (1996) 417.

[16] A.V. Radyushkin, private communication, 1997.

[17] I.D. King and C.T.Sachrajda, Nucl. Phys. **A598**(1987) 785 .

[18] V.L. Chernyak, A.A. Oglobin, and A.R. Zhitnitsky, Z. Phys. **C42**(1989) 569 .

[19] V.L. Chernyak and A.R. Zhitnitsky, Phys. Rep. **112**(1984) 173 .

[20] A. Afanasev at the Jefferson Laboratory/INT Workshop on Exclusive and Semi-Exclusive Processes at High Momentum Transfer, May 1999, and hep-ph/9808291.

[21] R. R. Crittenden, *et al.*, Nucl. Instr. and Meth. A **387**(1997) 377.

[22] J. L. Matthews and R. O. Owens, Nucl. Instr. and Meth. **111** (1973) 157.

[23] A. Afanasev, private communication.

[24] L. Andivahis, *et al.*, Phys. Rev. D **50** (1994) 5491; P. E. Bosted, *et al.*, Phys. Rev. Lett. **68** (1992) 3841.

Table 1: Kinematics for the proposed RCS measurements. E is the beam energy and $\bar{E}_\gamma$ is the mean photon energy in a 10% interval whose maximum energy is 0.1 GeV below E. D is the target-to-calorimeter distance needed to match the HRS acceptance.

| $E$ (GeV) | $\bar{E}_\gamma$ (GeV) | $s$ $(GeV)^2$ | $-t$ $(GeV^2)$ | $-u$ $(GeV^2)$ | $\theta_{cm}$ (deg) | D (m) | $\theta_\gamma$ (deg) | $E'_\gamma$ (GeV) | $\theta_p$ (deg) | $p_p$ (GeV) |
|---|---|---|---|---|---|---|---|---|---|---|
| 3.00 | 2.77 | 6.08 | 1.84 | 2.48 | 80. | 11.0 | 35.43 | 1.8 | 38.40 | 1.67 |
| 3.00 | 2.77 | 6.08 | 2.22 | 2.09 | 90. | 9.0 | 41.68 | 1.6 | 33.62 | 1.90 |
| 3.00 | 2.77 | 6.08 | 2.61 | 1.71 | 100. | 8.0 | 48.81 | 1.4 | 29.16 | 2.13 |
| 3.00 | 2.77 | 6.08 | 2.98 | 1.33 | 110. | 6.0 | 57.06 | 1.2 | 24.97 | 2.35 |
| 4.00 | 3.72 | 7.87 | 2.04 | 4.07 | 70. | 14.0 | 26.37 | 2.6 | 40.67 | 1.80 |
| 4.00 | 3.72 | 7.87 | 2.56 | 3.54 | 80. | 11.0 | 31.36 | 2.4 | 35.65 | 2.10 |
| 4.00 | 3.72 | 7.87 | 3.10 | 3.00 | 90. | 9.0 | 36.99 | 2.1 | 31.04 | 2.42 |
| 4.00 | 3.72 | 7.87 | 3.64 | 2.47 | 100. | 8.0 | 43.47 | 1.8 | 26.79 | 2.72 |
| 4.00 | 3.72 | 7.87 | 4.16 | 1.94 | 110. | 6.0 | 51.07 | 1.5 | 22.85 | 3.01 |
| 4.00 | 3.72 | 7.87 | 4.65 | 1.45 | 120. | 5.0 | 60.18 | 1.2 | 19.16 | 3.29 |
| 4.00 | 3.72 | 7.87 | 5.10 | 1.01 | 130. | 5.0 | 71.31 | 1.0 | 15.67 | 3.53 |
| 5.00 | 4.68 | 9.66 | 2.62 | 5.27 | 70. | 14.0 | 23.87 | 3.3 | 38.32 | 2.14 |
| 5.00 | 4.68 | 9.66 | 3.30 | 4.60 | 80. | 11.0 | 28.43 | 2.9 | 33.41 | 2.53 |
| 5.00 | 4.68 | 9.66 | 3.99 | 3.91 | 90. | 9.0 | 33.60 | 2.6 | 28.96 | 2.92 |
| 5.00 | 4.68 | 9.66 | 4.68 | 3.22 | 100. | 8.0 | 39.58 | 2.2 | 24.91 | 3.30 |
| 5.00 | 4.68 | 9.66 | 5.35 | 2.55 | 110. | 6.0 | 46.65 | 1.8 | 21.18 | 3.67 |
| 5.00 | 4.68 | 9.66 | 5.98 | 1.92 | 120. | 5.0 | 55.21 | 1.5 | 17.72 | 4.02 |
| 5.00 | 4.68 | 9.66 | 6.55 | 1.35 | 130. | 5.0 | 65.84 | 1.2 | 14.47 | 4.33 |
| 6.00 | 5.63 | 11.45 | 2.82 | 6.87 | 65. | 17.0 | 20.04 | 4.1 | 38.95 | 2.25 |
| 6.00 | 5.63 | 11.45 | 3.21 | 6.48 | 70. | 14.0 | 21.98 | 3.9 | 36.33 | 2.48 |
| 6.00 | 5.63 | 11.45 | 4.03 | 5.66 | 80. | 11.0 | 26.20 | 3.5 | 31.54 | 2.94 |
| 6.00 | 5.63 | 11.45 | 4.88 | 4.81 | 90. | 9.0 | 31.00 | 3.0 | 27.25 | 3.41 |
| 6.00 | 5.63 | 11.45 | 5.72 | 3.96 | 100. | 8.0 | 36.57 | 2.6 | 23.37 | 3.88 |
| 6.00 | 5.63 | 11.45 | 6.55 | 3.14 | 110. | 6.0 | 43.21 | 2.1 | 19.83 | 4.33 |

Table 2: Counting rates and backgrounds for the proposed measurements. The overall angular resolution is given in columns 4 and 5. The yield of Compton events is given in column 6. The ratio of $\pi^0$ , $ep$, and $ep\gamma$ to Compton events are given in column 7-9, respectively, and the projected time to achieve 5% statistics for Compton events is in the last column.

| $E$ GeV | $\bar{E}_\gamma$ GeV | $\theta_{cm}$ deg | $\sigma_\theta$ mr | $\sigma_o$ mr | $Y_{\gamma\gamma}$ ev/hr | $\pi^0/\gamma\gamma$ | $ep/\gamma\gamma$ | $ep\gamma/\gamma\gamma$ | T hr |
|---|---|---|---|---|---|---|---|---|---|
| 3.00 | 2.77 | 80. | 3.4 | 1.7 | 2345. | .57 | 16.85 | .102 | 0.3 |
| 3.00 | 2.77 | 90. | 3.5 | 2.0 | 1871. | .55 | 11.18 | .073 | 0.3 |
| 3.00 | 2.77 | 100. | 3.8 | 2.4 | 1420. | .54 | 7.88 | .054 | 0.4 |
| 3.00 | 2.77 | 110. | 4.2 | 3.0 | 1409. | .54 | 5.78 | .045 | 0.4 |
| 4.00 | 3.72 | 70. | 3.0 | 1.2 | 1144. | .58 | 30.39 | .174 | 0.6 |
| 4.00 | 3.72 | 80. | 3.1 | 1.4 | 881. | .57 | 18.89 | .114 | 0.7 |
| 4.00 | 3.72 | 90. | 3.2 | 1.7 | 668. | .57 | 12.57 | .079 | 0.9 |
| 4.00 | 3.72 | 100. | 3.5 | 2.1 | 498. | .56 | 8.69 | .058 | 1.3 |
| 4.00 | 3.72 | 110. | 4.0 | 2.6 | 467. | .57 | 6.31 | .047 | 1.3 |
| 4.00 | 3.72 | 120. | 4.6 | 3.4 | 369. | .58 | 4.65 | .038 | 1.7 |
| 4.00 | 3.72 | 130. | 5.5 | 4.3 | 242. | .57 | 3.50 | .034 | 2.6 |
| 5.00 | 4.68 | 70. | 2.8 | 1.0 | 523. | .59 | 32.83 | .186 | 1.2 |
| 5.00 | 4.68 | 80. | 2.9 | 1.2 | 387. | .60 | 20.68 | .123 | 1.6 |
| 5.00 | 4.68 | 90. | 3.1 | 1.5 | 284. | .60 | 14.22 | .088 | 2.3 |
| 5.00 | 4.68 | 100. | 3.4 | 1.9 | 207. | .60 | 9.88 | .067 | 3.1 |
| 5.00 | 4.68 | 110. | 3.9 | 2.5 | 176. | .62 | 7.15 | .052 | 3.7 |
| 5.00 | 4.68 | 120. | 4.5 | 3.2 | 135. | .63 | 5.32 | .043 | 4.8 |
| 5.00 | 4.68 | 130. | 5.4 | 4.2 | 85. | .62 | 3.98 | .038 | 7.6 |
| 6.00 | 5.63 | 65. | 2.6 | 0.8 | 316. | .61 | 46.47 | .262 | 2.0 |
| 6.00 | 5.63 | 70. | 2.6 | 0.9 | 262. | .62 | 36.21 | .205 | 2.5 |
| 6.00 | 5.63 | 80. | 2.8 | 1.1 | 184. | .63 | 23.63 | .141 | 3.6 |
| 6.00 | 5.63 | 90. | 3.0 | 1.4 | 138. | .65 | 15.97 | .099 | 4.8 |
| 6.00 | 5.63 | 100. | 3.3 | 1.8 | 97. | .65 | 11.27 | .076 | 6.8 |
| 6.00 | 5.63 | 110. | 3.8 | 2.4 | 75. | .68 | 8.36 | .061 | 8.9 |

Table 3: Summary of beam request for the unpolarized and polarized RCS measurements. The numbers listed are times in hours.

| | unpolarized | polarized | TOTAL |
|---|---|---|---|
| running time | 65 | 173 | 238 |
| calibrations | 128 | 20 | 148 |
| configuration changes | 52 | 0 | 52 |
| TOTAL | 245 | 193 | 438 |

Table 1: Kinematics for the proposed RCS measurements. E is the beam energy and $\bar{E}_\gamma$ is the mean photon energy in a 10% interval whose maximum energy is 0.1 GeV below E. D is the target-to-calorimeter distance needed to match the HRS acceptance.

| $E$ (GeV) | $\bar{E}_\gamma$ (GeV) | $s$ (GeV)² | $-t$ (GeV²) | $-u$ (GeV²) | $\theta_{cm}$ (deg) | $D$ (m) | $\theta_\gamma$ (deg) | $E'_\gamma$ (GeV) | $\theta_p$ (deg) | $p_p$ (GeV) |
|---|---|---|---|---|---|---|---|---|---|---|
| 3.00 | 2.77 | 6.08 | 1.84 | 2.48 | 80. | 11.0 | 35.43 | 1.8 | 38.40 | 1.67 |
| 3.00 | 2.77 | 6.08 | 2.22 | 2.09 | 90. | 9.0 | 41.68 | 1.6 | 33.62 | 1.90 |
| 3.00 | 2.77 | 6.08 | 2.61 | 1.71 | 100. | 8.0 | 48.81 | 1.4 | 29.16 | 2.13 |
| 3.00 | 2.77 | 6.08 | 2.98 | 1.33 | 110. | 6.0 | 57.06 | 1.2 | 24.97 | 2.35 |
| 4.00 | 3.72 | 7.87 | 2.04 | 4.07 | 70. | 14.0 | 26.37 | 2.6 | 40.67 | 1.80 |
| 4.00 | 3.72 | 7.87 | 2.56 | 3.54 | 80. | 11.0 | 31.36 | 2.4 | 35.65 | 2.10 |
| 4.00 | 3.72 | 7.87 | 3.10 | 3.00 | 90. | 9.0 | 36.99 | 2.1 | 31.04 | 2.42 |
| 4.00 | 3.72 | 7.87 | 3.64 | 2.47 | 100. | 8.0 | 43.47 | 1.8 | 26.79 | 2.72 |
| 4.00 | 3.72 | 7.87 | 4.16 | 1.94 | 110. | 6.0 | 51.07 | 1.5 | 22.85 | 3.01 |
| 4.00 | 3.72 | 7.87 | 4.65 | 1.45 | 120. | 5.0 | 60.18 | 1.2 | 19.16 | 3.29 |
| 4.00 | 3.72 | 7.87 | 5.10 | 1.01 | 130. | 5.0 | 71.31 | 1.0 | 15.67 | 3.53 |
| 5.00 | 4.68 | 9.66 | 2.62 | 5.27 | 70. | 14.0 | 23.87 | 3.3 | 38.32 | 2.14 |
| 5.00 | 4.68 | 9.66 | 3.30 | 4.60 | 80. | 11.0 | 28.43 | 2.9 | 33.41 | 2.53 |
| 5.00 | 4.68 | 9.66 | 3.99 | 3.91 | 90. | 9.0 | 33.60 | 2.6 | 28.96 | 2.92 |
| 5.00 | 4.68 | 9.66 | 4.68 | 3.22 | 100. | 8.0 | 39.58 | 2.2 | 24.91 | 3.30 |
| 5.00 | 4.68 | 9.66 | 5.35 | 2.55 | 110. | 6.0 | 46.65 | 1.8 | 21.18 | 3.67 |
| 5.00 | 4.68 | 9.66 | 5.98 | 1.92 | 120. | 5.0 | 55.21 | 1.5 | 17.72 | 4.02 |
| 5.00 | 4.68 | 9.66 | 6.55 | 1.35 | 130. | 5.0 | 65.84 | 1.2 | 14.47 | 4.33 |
| 6.00 | 5.63 | 11.45 | 2.82 | 6.87 | 65. | 17.0 | 20.04 | 4.1 | 38.95 | 2.25 |
| 6.00 | 5.63 | 11.45 | 3.21 | 6.48 | 70. | 14.0 | 21.98 | 3.9 | 36.33 | 2.48 |
| 6.00 | 5.63 | 11.45 | 4.03 | 5.66 | 80. | 11.0 | 26.20 | 3.5 | 31.54 | 2.94 |
| 6.00 | 5.63 | 11.45 | 4.88 | 4.81 | 90. | 9.0 | 31.00 | 3.0 | 27.25 | 3.41 |
| 6.00 | 5.63 | 11.45 | 5.72 | 3.96 | 100. | 8.0 | 36.57 | 2.6 | 23.37 | 3.88 |
| 6.00 | 5.63 | 11.45 | 6.55 | 3.14 | 110. | 6.0 | 43.21 | 2.1 | 19.83 | 4.33 |

Table 2: Counting rates and backgrounds for the proposed measurements. The overall angular resolution is given in columns 4 and 5. The yield of Compton events is given in column 6. The ratio of $\pi^0$, $ep$, and $ep\gamma$ to Compton events are given in column 7-9, respectively, and the projected time to achieve 5% statistics for Compton events is in the last column.

| $E$ GeV | $\bar{E}_\gamma$ GeV | $\theta_{cm}$ deg | $\sigma_\theta$ mr | $\sigma_\phi$ mr | $Y_{\gamma\gamma}$ ev/hr | $\pi^0/\gamma\gamma$ | $ep/\gamma\gamma$ | $ep\gamma/\gamma\gamma$ | $T$ hr |
|---|---|---|---|---|---|---|---|---|---|
| 3.00 | 2.77 | 80. | 3.4 | 1.7 | 2345. | .57 | 16.85 | .102 | 0.3 |
| 3.00 | 2.77 | 90. | 3.5 | 2.0 | 1871. | .55 | 11.18 | .073 | 0.3 |
| 3.00 | 2.77 | 100. | 3.8 | 2.4 | 1420. | .54 | 7.88 | .054 | 0.4 |
| 3.00 | 2.77 | 110. | 4.2 | 3.0 | 1409. | .54 | 5.78 | .045 | 0.4 |
| 4.00 | 3.72 | 70. | 3.0 | 1.2 | 1144. | .58 | 30.39 | .174 | 0.6 |
| 4.00 | 3.72 | 80. | 3.1 | 1.4 | 881. | .57 | 18.89 | .114 | 0.7 |
| 4.00 | 3.72 | 90. | 3.2 | 1.7 | 668. | .57 | 12.57 | .079 | 0.9 |
| 4.00 | 3.72 | 100. | 3.5 | 2.1 | 498. | .56 | 8.69 | .058 | 1.3 |
| 4.00 | 3.72 | 110. | 4.0 | 2.6 | 467. | .57 | 6.31 | .047 | 1.3 |
| 4.00 | 3.72 | 120. | 4.6 | 3.4 | 369. | .58 | 4.65 | .038 | 1.7 |
| 4.00 | 3.72 | 130. | 5.5 | 4.3 | 242. | .57 | 3.50 | .034 | 2.6 |
| 5.00 | 4.68 | 70. | 2.8 | 1.0 | 523. | .59 | 32.83 | .186 | 1.2 |
| 5.00 | 4.68 | 80. | 2.9 | 1.2 | 387. | .60 | 20.68 | .123 | 1.6 |
| 5.00 | 4.68 | 90. | 3.1 | 1.5 | 284. | .60 | 14.22 | .088 | 2.3 |
| 5.00 | 4.68 | 100. | 3.4 | 1.9 | 207. | .60 | 9.88 | .067 | 3.1 |
| 5.00 | 4.68 | 110. | 3.9 | 2.5 | 176. | .62 | 7.15 | .052 | 3.7 |
| 5.00 | 4.68 | 120. | 4.5 | 3.2 | 135. | .63 | 5.32 | .043 | 4.8 |
| 5.00 | 4.68 | 130. | 5.4 | 4.2 | 85. | .62 | 3.98 | .038 | 7.6 |
| 6.00 | 5.63 | 65. | 2.6 | 0.8 | 316. | .61 | 46.47 | .262 | 2.0 |
| 6.00 | 5.63 | 70. | 2.6 | 0.9 | 262. | .62 | 36.21 | .205 | 2.5 |
| 6.00 | 5.63 | 80. | 2.8 | 1.1 | 184. | .63 | 23.63 | .141 | 3.6 |
| 6.00 | 5.63 | 90. | 3.0 | 1.4 | 138. | .65 | 15.97 | .099 | 4.8 |
| 6.00 | 5.63 | 100. | 3.3 | 1.8 | 97. | .65 | 11.27 | .076 | 6.8 |
| 6.00 | 5.63 | 110. | 3.8 | 2.4 | 75. | .68 | 8.36 | .061 | 8.9 |

Table 3: Summary of beam request for the unpolarized and polarized RCS measurements. The numbers listed are times in hours.

| | unpolarized | polarized | TOTAL |
|---|---|---|---|
| running time | 65 | 173 | 238 |
| calibrations | 128 | 20 | 148 |
| configuration changes | 52 | 0 | 52 |
| TOTAL | 245 | 193 | 438 |

## 3.7 Luminosity Considerations

We now address the issue of luminosity limitations imposed by the counting rates in the photon arm. Our approach has been to do measurements in some limited kinematic range and then use a Monte Carlo code to extrapolate into other regions. The code we have used was designed for radiation shielding calculations and uses the DINREG event generator in the framework of GEANT detector simulations and particle transport code. The measurements were discussed in Section 3.2. At 4 GeV and 35°, the measured counting rates and energy flows were comparable, although less than, those predicted by the code.

With the Monte Carlo code reasonably calibrated, we now use it to extrapolate to kinematics and luminosities of interest to the Compton experiment, for which we will use a copper radiator of thickness 0.8 g/cm$^2$ (6% radiation length), a scattering target of 1 g/cm$^2$ Hydrogen, and a beam of intensity 10 $\mu$A. The worst case situation is the 6 GeV point at $\theta_{cm} = 65°$, for which the calorimeter is at $\theta_{lab} \sim 20°$ and the scattered photons/electrons have an energy of 4.3 GeV. Assuming a 1 m$^2$ detector at 17 m, the code predicts a total rate (electrons plus photons) of 4 MHz above 0.5 GeV and 0.5 MHz above 2 GeV. Given the high segmentation of the calorimeter and veto detectors, this should be a tolerable rate.

## 3.8 Counting Rate Estimates

The RCS event rate is given by

$$\frac{dN_{\gamma\gamma}}{dt} = TX \left[\frac{I}{e}\right] \frac{d\sigma}{d\Omega_p} \frac{\Delta E_\gamma \Delta\Omega_p}{\bar{E}_\gamma}, \qquad (19)$$

where $T$ is the target thickness, $X$ is the radiator thickness, $I$ is the beam current, $-e$ is the electron charge, $\bar{E}_\gamma$ is the mean incident photon energy over the acceptance interval $\Delta E_\gamma$, and $\Delta\Omega_p$ is the angular acceptance of the proton spectrometer. Rate estimates in counts/hour are given in Table 2. These estimates assume a 15-cm long liquid Hydrogen target ($T = 6.3 \times 10^{23} cm^{-2}$), a 6% radiator ($X = 0.06$), a modest beam current of 10 $\mu$A, and the standard HRS acceptances (51 mr and 102 mr for for the horizontal and vertical angles, ±4.5% in momentum, and ±3 cm in $y$). The calculation of the rates takes into account the geometrical acceptance of the calorimeter and uses the RCS cross section of Eq. 7 and Fig. 4. Also shown in Table 2 are the expected backgrounds due to the $\pi^0$ photons, $ep$, and $ep\gamma$.

For the polarization transfer measurement at E=4 GeV, $\theta_{cm}=110°$, the recoil proton momentum is 3.0 GeV/c. A longitudinally polarized photon beam is required. We assume polarization transferred to the bremsstrahlung photon according to the formula [23]

$$\frac{P_\gamma}{P_e} = \frac{y(4 - y)}{4 - 4y + 3y^2}, \qquad (20)$$

where $y = E_\gamma/E = 0.93$ for the proposed measurement. Therefore we can expect $P_\gamma$ to be about 99% of $P_e$. We assume an electron polarization of 70%, which is currently being achieved in the Happex experiment. We further assume the same FPP characteristics as that assumed for E99-007, with the analyzer upgraded to 70 cm of polyethylene, which implies a figure of merit $\epsilon A_y^2 \approx 0.01$ at 3.0 GeV/c. Using the standard formula for the uncertainty in the measured polarization $\sigma_P$

$$\sigma_P = \frac{\pi}{2 A_y P_\gamma \sqrt{N\epsilon}}, \qquad (21)$$

where N is the number of events, we will need N=50,000 events to achieve a precision of $\sigma_P$=0.1. At this recoil momentum, the spin precession is 270° so that the measurement will have maximum sensitivity to the longitudinal component of the recoil polarization at the target and no sensitivity to the normal component. Referring to the counting rates in Table 2, and taking into account the $\pi^0$ background, it will therefore require 173 hours of beam to determine both $A_{LL}$ and $A_{LT}$ with a precision of 0.1. Using Eq. 11 and Diehl's model for $R_V$, this will determine $R_A$ to an absolute precision of ±0.01.

It would be desirable to extend the polarization measurements to higher energy. Since both the cross sections and the FPP figure of merit fall as the energy goes up, the measurements become very time consuming. For example, to achieve a precision of 0.1 in the transverse polarization at E=5 GeV, $-t$=5 requires approximately 600 hours of beam while E=5 GeV, $-t$=6 requires over 1200 hours. For such measurements, it might be preferable to use a polarized target rather than detect the recoil polarization, in which case it would be necessary to develop techniques that would allow a clean photon beam on the target.

## 3.9 Calibrations and Systematic Errors

Our goal is to measure the Compton scattering cross section to a statistical precision of 5% and with overall systematic uncertainty on the order of 6%. In this section, we outline one possible calibration procedure, with particular attention to techniques to reduce the systematic errors.

Our plan is to measure the RCS cross section relative to the $ep$ elastic cross section, which is experimentally measured to better than 3.5% [24]. For each kinematic point, we do measurements with the deflection magnet both on (MON) and off (MOFF). Since the kinematics of RCS and $ep$ elastic are essentially identical, the same cuts on the HRS spectrometer can be used to select RCS events only (MON) or RCS plus $ep$ events (MOFF), or just $ep$ for MOFF events accompanied by a veto signal. Designating R as the measured ratio of RCS to $ep$ events, we have

$$\left(\frac{d\sigma}{dt}\right)_{RCS} = R \frac{N_\gamma}{N_e} \left(\frac{d\sigma}{dt}\right)_{ep}, \qquad (22)$$

where $N_\gamma$ and $N_e$ are the number of incident photons and electrons, respectively, after passing through the 6% radiator. This technique of normalization is very appealing since it is independent of the acceptances of both the calorimeter and the HRS. Moreover it is insensitive to all effects associated with electron beam monitoring, target thickness, and data acquisition deadtime, as long as these effects are the same for the MON and MOFF runs. The cost of using this technique is that supplemental measurements must be done to determine $N_e$, the post-radiator energy spectrum of electrons. We propose measuring this with $ep$ elastic scattering using the pair of HRS spectrometers. By doing this measurement with and without a radiator, one can measure the number of energy-degraded post-radiator electrons per incident electron in the energy region of interest near the bremsstrahlung endpoint, with an accuracy of about 3.5%. We plan to do this measurement at two of the four energies in order to check and calibrate our calculation of $N_e$, which will be used at the other two energies.

Additional calibrations will be done once for each of the four beam energies at the most forward calorimeter angle:

1. Calibrations of the energy and position response of the calorimeter using $ep$ elastic scattering without a radiator and with the deflection magnet turned off. These measurements also utilize the MWPC for a precise position measurement.

Based on the feasibility measurements, we expect calorimeter trigger rates to be less than about 1 Mhz. With a coincidence resolving time of 10 ns, this implies less than 1% accidental coincidences. If necessary, this can be further reduced by taking advantage of the spatial correlation between the recoil proton and scattered photon and having a TDC for each 16 x 2 subarray.

The detector platform needs to be designed to allow quick changes of scattering angle as well as radial distance to the target. Since the position of the detector will be calibrated at each kinematic setting, the alignment requirements can be relaxed considerably. We are presently considering a standalone assembly consisting of a large stand that is positioned in Hall A with air pads. The detector will be surveyed relative to alignment fiducials on the base of the stand, which will then be positioned with respect to fixed marks on the floor of the hall.

## 3.4   Background from $\pi^0$ Photons

The goal is to separate the $p(\gamma, \gamma' p)$ events from the $p(\gamma, \pi^0 p)$ events. Because of the small mass of the pion, the four-momentum of a coherently produced $\pi^0$ is nearly identical to that of a Compton photon. For a monochromatic incident photon beam, it would be possible to resolve Compton from $\pi^0$ events by a precise measurement of the three-momentum of the recoil proton (indeed, this is essentially the technique used in the VCS experiments), but this will not work for a continuous bremsstrahlung spectrum. Instead one relies on the kinematic correlation between the recoil proton and the associated Compton photon or $\pi^0$ . Under the assumption of two-body kinematics, a measurement of the three-momentum of the recoil proton uniquely defines both the energy of the photon that initiated the event and the three-momentum of the photon or $\pi^0$ . The $\pi^0$ decays into two photons. The higher energy photon has an energy between $E_\pi/2$ and $E_\pi \approx E'_\gamma$ (the energy of a scattered photon in the same kinematics) and is confined to a cone of half-angle $m_\pi/E_\pi$ about the pion direction. The lower energy photon has an energy less than $E_\pi/2$ and lies outside the cone. In contrast, for fixed kinematics of the recoil, the Compton photon is spread out in solid angle only by the overall angular resolution of the coincidence detection system. This resolution is determined by the intrinsic resolution of the magnetic spectrometer for the in-plane and out-of-plane proton angles and for vertex reconstruction; by proton multiple scattering in the target and other material; by the angular spread of the incident photon beam; and by and the ability of the calorimeter to determine the angle of the scattered photon. We combine all these effects into effective Compton angular resolutions, which we denote by $\sigma_\theta$ and $\sigma_\phi$ for the horizontal and vertical directions, respectively. The ratio $R_{\pi^0}$ of coherent $\pi^0$ photons to Compton photons is therefore determined by the ratio of cross sections divided by the fraction of the $\pi^0$ photons falling within the angular resolution. One easily finds

$$R_{\pi^0} = 11 \frac{d\sigma(\gamma, \pi^0)}{d\sigma(\gamma, \gamma)} \frac{\sigma_\theta \sigma_\phi}{(m_\pi/E'_\gamma)^2},$$   (17)

where the numerical factor comes in part from the fraction of Compton events within $2\sigma$ of a two-dimensional Gaussian distribution.

We see then that the Compton and $\pi^0$ events are distinguished by the distributions of $\delta\theta_\gamma$ and $\delta\phi_\gamma$ which are, respectively, the difference between the measured photon angles and those photon angles reconstructed based on the measurement of the proton kinematics. Typical distributions of these quantities measured in the feasibility experiment are shown in Fig. 11. The resolutions in these quantities, $\sigma_\theta$ and $\sigma_\phi$, respectively, directly enter into the expression for $R_{\pi^0}$ given above. It is important to note that enough of the $\pi^0$ photon distribution can be measured in the experiment to interpolate the distribution accurately under the Compton peak. Therefore, the running time

needed to obtain a given statistical precision in the measurement of the Compton cross section is proportional to $1+R_{\pi^0}$ .

As an example, we present a detailed estimate of $\sigma_\phi$ and $\sigma_\theta$ for the specific case of 6 GeV at 110°. The quantity $\sigma_\phi$ has contributions from the following:

- $\sigma_x^\gamma$, the position resolution of the calorimeter. We assume this to be 5 mm, as discussed earlier. At a distance of 6 m (determined by the horizontal angular acceptance), this contributes 0.8 mr to $\sigma_\phi$.

- $\sigma_\phi^p$, the out-of-plane angular resolution of the HRS, which we take to be 0.9 mr, a value that has already been achieved. This leads to a contribution to $\sigma_\phi$ of 1.8 mr.

- The proton multiple scattering in the target. This is calculated using standard formulas, taking into account the hydrogen in the target, the aluminum wall of the target can, and the exit aluminum foil to the scattering chamber. Together these contribute 0.8 mr.

- The vertical angular spread of the photon beam. This is calculated assuming it is due to multiple scattering by the electron beam in the radiator. It contributes 1.0 mr.

- The vertical beam spot size. We calculate this by assuming the spot size is due to the angular spread and therefore less than 1 mm. It contributes 0.8 mr.

Similarly, $\sigma_\theta$ has contributions from the following:

- $\sigma_x^\gamma$, the position resolution of the calorimeter. Once again, this contributes 0.8 mr.

- $\sigma_\theta^p$, the in-plane angular resolution of the HRS, which we take to be 0.9 mr, a value that has already been achieved. This leads to a contribution of 3.3 mr.

- the proton multiple scattering in the target. This contributes 1.4 mr.

- The horizontal angular spread of the photon beam. This contributes 1.0 mr.

- The horizontal beam spot size. This contributes 0.1 mr.

- $\sigma_y^p$, the resolution in proton vertex reconstruction transverse to the spectrometer axis. We use the value 0.7 mm that has been achieved, leading to a contribution of 0.3 mr.

- $\sigma_p$, the proton momentum resolution. This contributes negligibly.

Combining these independent contributions in quadrature, we find $\sigma_\theta$=3.8 mr and $\sigma_\phi$=2.5 mr. By comparison, the Cornell experiment achieved 8.5 in $\theta$ and 2.1 in $\phi$. The above number show that these results are dominated by contributions from the HRS, $\sigma_\theta^p$ and $\sigma_\phi^p$, so that is where any improvements should be aimed. The resolutions calculated for all our proposed kinematics are given in Table 2.

To calculate $R_{\pi^0}$ , we use the expression of Eq. 7 for the RCS cross section, with form factors from Fig. 4. For the $p(\gamma, \pi^0 p)$ cross section, we assume

$$\frac{d\sigma(\gamma, \pi^0)}{dt} = 40 \frac{8.4 \, GeV^2}{s} \frac{d\sigma(\gamma, \gamma)}{dt},$$   (18)

where the numerical factor comes from the Cornell data and the $s$-dependence is that expected from asymptotic scaling. In Table 2, we see that $R_{\pi^0} \approx 0.6$, essentially independent of our kinematics. The worse angular resolution at backward angles (as the detector moves closer to the target) is compensated by the larger $\pi^0$ cone.
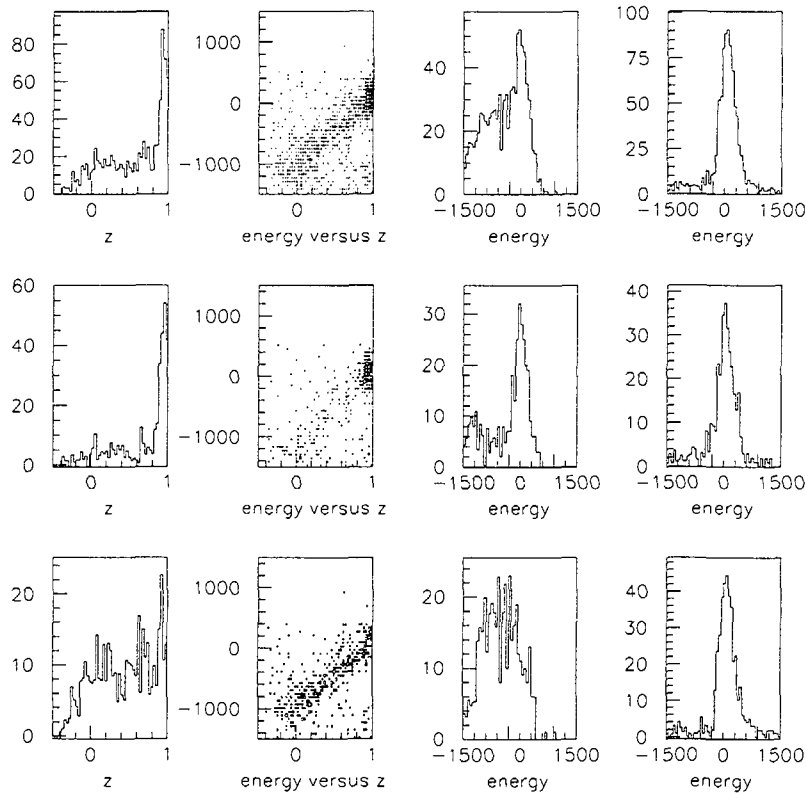
Figure 13: *Energy and angular plots for coincidence events with the 6% radiator and 4 cm LH₂ target. The top row includes all the selected coincidence events, whereas the middle and bottom rows are those selected events satisfying the electron and photon cuts, respectively, in the veto detector. For each row, the first column is the parameter z, which is the cosine of the $\pi^0$ decay angle in its rest frame relative to the $\pi^0$ direction in the Lab and is reconstructed from the proton kinematics and photon angle measured in the calorimeter. The third column is the difference between the measured photon energy and that reconstructed based on ep kinematics. The second column is a scatter plot of the energy difference and z. The fourth column is the difference between the measured photon energy and that reconstructed based on $(\gamma, \pi^0)$ kinematics (using the z information). In the z distribution, the peak near z = 1 comes from events having two-body kinematics, primarily ep scattering and RCS.*
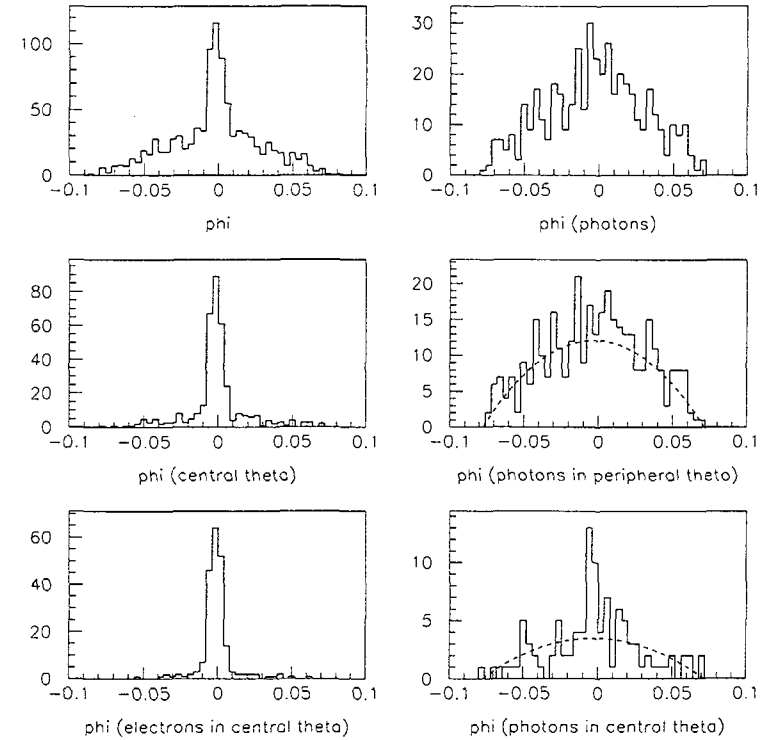


Figure 14: *Proof of principle experiment for RCS at 4 GeV and $\theta_{cm} \simeq 90°$. All panels show the difference between the measured out-of-plane angle $\phi$ in the calorimeter and the reconstructed angle based on the HRS measurement and two-body kinematics. The upper left panel shows all coincidence events. The peak at $\phi = 0$ is due primarily to ep scattering and secondarily to RCS, whereas the continuum is due to $\pi^0$ decay photons. For the middle left panel, a cut is made requiring that the in-plane angle $\theta$ be close to that expected for two-body kinematics; this clearly enhances the central peak. The lower left panel in addition demands a signal in the veto detector, thereby selective picking out the ep events. The right panels demand no signal in the veto, thereby picking out photons. An anti-cut on the in-plane angle (middle right) preferentially picks out $\pi^0$ decay photons, whereas a cut on the in-plane angle (bottom right) selectively enhances the RCS events, with some continuum mixed in. Therefore, the events above the dashed line in the lower right panel represent RCS events, with a 10% contamination due to the inefficiency of the veto detector. The number of RCS events agree within statistics with the Cornell measurements.*

with the recoil proton relative to undeflected RCS photons. The mixed $\gamma - e$ beam is advantageous in that the $ep$ electrons can be used to calibrate the photon spectrometer. For this purpose, several planes of MWPC just in front of the calorimeter will be used in a separate *in situ ep* elastic scattering experiment to calibrate the position of each element of the calorimeter and veto detector, measure the position resolution, and measure the veto efficiency. The data acquisition electronics will utilize a variety of commercial NIM, CAMAC, and FASTBUS modules as well as some custom designed modules for the fast trigger. The entire spectrometer will be mounted on a mechanical assembly that allows changes in both scattering angle and radial distance, the latter needed to match the photon acceptance to that of the proton at different kinematic settings.

The kinematics we have chosen to investigate is shown in Fig. 8 as well as in Tables 1 and 2. Specifically, we propose 24 measurements that are arranged in order to study the $s$-dependence of the cross section at five center-of-mass scattering angles in the range $70°$-$110°$; to study the behavior of the cross section at fixed -$t$ in the range 2-6 GeV$^2$; and to study the $t$-dependence of the cross section at the fixed $s$ corresponding to 4, 5, and 6 GeV beams. The angular limits of the 6 GeV measurements are dictated on the low end ($\theta_{cm} = 70°$) by the need to keep the photon detector at a laboratory angle no smaller than $20°$ due to the severe increase in background of low energy electrons and photons below that angle, and on the high side by the maximum momentum accessible with the HRS (4.5 GeV for the spectrometer normally used as the electron arm). For the recoil polarization transfer experiment, a single measurement at E=4 GeV, $\theta_{cm}$=90° (-$t$=3 GeV$^2$) is planned.

The technique we will use is conceptually identical to that used in the Cornell experiment. However, the combined effects of a high quality, high duty factor electron beam, a state-of-the-art magnetic spectrometer, the ability to calibrate *in situ* with $ep$ elastic scattering, and high segmentation in the photon detector should allow significantly better measurements in the range of $s$ and $t$ already covered by Cornell, as well as significant extensions beyond that. The equipment would also be suitable for measurements at higher energies, should those energies become available at JLab in the future.

## 3.2  Results of Feasibility Studies

During 1998, a prototype photon spectrometer was built and tested with both parasitic and dedicated beam time at JLab. In effect, a small-scale model of the full detector was constructed and used in a real experiment. The principal components of the prototype were as follows: a calorimeter consisting of a 20x20 cm$^2$ array of lead glass blocks of type TF-1, each detector with dimensions 4x4x40 cm$^3$; two planes of veto hodoscope, one vertical and one horizontal, each composed of 4 cm wide x 10 cm long x 4 cm thick strips of plastic scintillator; and two planes of MWPC with 1 mm wire spacing. Most of the tests utilized a 4.1 GeV electron beam, with currents ranging from a few to 60 $\mu$A, with the photon detector at about 35° and 10 m from the target. The target options included a 15 cm and 4 cm LH$_2$ targets, the latter equipped with a 6% Cu radiator 26 cm from the target center. The photon electronics were fully incorporated into the Hall A data acquisition, allowing the detection of coincidences with the hadron HRS and full readout of both the photon spectrometer and HRS detector package. The only missing component in the setup was a suitable deflection magnet. The results of the tests are summarized as follows:

1. For scattering angles as small as 20°, the minimum anticipated, and at luminosities appropriate for the actual RCS experiment, the calorimeter operated in a stable manner with no significant deterioration of the energy or position resolution. Indeed, the measured counting rates and energy flows were generally about a factor of two below those predicted by a detailed Monte-Carlo

calculation. Therefore the desired luminosities can be achieved with no loss of performance of the calorimeter. Moreover, the measurements show *no noticeable degradation* (i.e., $\leq$ 2%) in the pulse height of the calorimeter blocks after a radiation dose approximately half that expected for the entire RCS experiment, thereby obviating the need to use radiation hardened lead glass.

2. A position resolution $\sigma_x \approx$ 5.4 mm and an energy resolution $\sigma_E/E \approx$ 4.6% (see Fig. 10)were achieved for $\approx$ 2.2 GeV electrons, both of which are sufficient for the experiment. The position resolution contributed only 0.6 mr to the overall angular resolution, which was measured to be about 2.8 and 3.2 mr for the in-plane and out-of-plane angles, respectively (see Fig. 11) and was dominated by the hadron arm. Although adequate for the RCS experiment (see Section 3.4), improved HRS angular resolution is desirable. Coincidences between the HRS and calorimeter provide an excellent technique to measure and optimize the HRS angular resolution, and an attempt will be made to do so in the near future.

3. The MWPC works as a calibration device for currents up to 5 $\mu$A. It was used to measure the position resolution of the calorimeter. A new prototype chamber has been built and will be tested during summer 1999, with the goal of using it as part of the veto detector during the RCS experiment itself rather than just as a calibration detector.

4. It was determined that segmentation of the veto detector is essential in view of the large counting rates. The initial choice of 4-cm thick plastic scintillators has been successful. Despite the high counting rates, the veto provided efficient discrimination against electrons. However, it is likely that a plexiglass Čerenkov detector will be even more effective in view of its reduced sensitivity to low velocity particles, and tests of these detectors under realistic beam conditions are in progress.

5. At luminosities needed for RCS, the raw coincidence spectrum between the calorimeter and HRS is very clean (see Fig. 12) under realistic running conditions for the kinematics $s \approx$ 8 and $-t \approx$ 3 GeV$^2$. Moreover, it is clear that this can be improved further both by appropriate cuts in the proton and photon kinematics and by matching the timing of each Pb-glass block. We conclude that chance coincidences will not be a problem for the RCS experiment.

6. As a "proof of principle", the actual RCS experiment was performed, the results of which are summarized in Figs. 13 and 14. The conclusions are that the $\pi^0$ background is understood and under control; that the mixed photon-electron beam can be dealt with and is actually a desirable feature in that it allows *in situ* calibrations; that the background in the hadron HRS when working at photon energies below the bremsstrahlung endpoint are manageable; and that the experiment is feasible with the planned equipment.

## 3.3  Photon Spectrometer

The key new piece of instrumentation is the photon calorimeter, which will consist of 702 lead-glass blocks of type TF-1, the identical blocks that have performed so well during the feasibility experiment. As already remarked, the feasibility studies have shown that radiation hardened lead glass is not necessary for the RCS experiment. The array of blocks, each with dimensions 4x4x40 cm$^3$ and with an expected position resolution of order 5 mm, will be arranged into an rectangular array of 26 columns by 27 rows (approximately 1m x 1m). All lead glass and PMT's will be provided by the Yerevan collaborators. A total of 200 blocks and PMT's are already at Jlab and the remainder will be delivered during 1999. A design for packaging the blocks into a working calorimeter, including design of the PMT bases, is complete and construction is in progress.

It is desirable to match the angular acceptance of the calorimeter to that of the proton arm. In

nearly independent of the energy. For scattering from the proton, $A_{LL}$ will be diminished by the ratio $R_A/R_V$, but to the extent that these two functions track together with $t$, one expects $A_{LL}$ to be nearly independent of energy also. The handbag prediction at 4 GeV is shown in Fig. 7, along with pQCD predictions with various DA's [3]. The difference between the two mechanisms is remarkable. One of the goals of this proposal is to measure $A_{LL}$ at the fixed kinematics of 4 GeV, 110° ($-t$=4 GeV$^2$) in order to test the reaction mechanism and determine $R_A$ with an accuracy shown in Fig. 4.

The transverse polarization transfer observable $A_{LT}$ is defined by

$$A_{LT}\frac{d\sigma}{dt} \equiv \frac{d\sigma(\uparrow\rightarrow)}{dt} - \frac{d\sigma(\uparrow\leftarrow)}{dt} \tag{14}$$

where the first arrow refers to the incident photon helicity and the second to the recoil proton transverse polarization (normal to the proton motion and in the scattering plane). This observable arises as an interference between proton helicity flip and helicity non-flip amplitudes. In the strict pQCD limit, it must vanish since hadron helicity is conserved. Thus far this observable has not been calculated with either the pQCD or handbag mechanisms. However, one can anticipate that in the handbag mechanism, it will be proportional to $R_T$, the RCS form factor that is closely related to the Pauli elastic form factor $F_2$. Both are derived from the ND $\mathcal{K}^a(x;t)$, which is an object of intense current interest [20] since it is related to the contribution of quark orbital angular momentum to the proton spin. Indeed it was the original motivation [9] for the development of the concept of non-forward parton distributions. This interest was further stimulated by the recent results from experiment 93-027, a measurement of $G_{E_p}/G_{M_p}$, which shows that $Q^2F_2/F_1$=1.3 and is still rising at $Q^2$=3.5 GeV$^2$, contrary to the pQCD prediction that it saturates at 1. Another goal of the present proposal is to measure $A_{LT}$ at the one fixed point in order to learn additional information about the importance of helicity flip amplitudes in exclusive processes and perhaps measure the RCS form factor $R_T$.

The induced polarization $P_N$ is the component of recoil polarization normal to the scattering plane and involves the imaginary part of the interference between helicity flip and nonflip amplitudes. In the handbag mechanism, it is suppressed since all amplitudes are strictly real in this model [7]. In the strict pQCD limit, it vanishes due to hadron helicity conservation. No calculation has yet been done for this quantity.

Experimentally, one can in principle measure all three components of the proton polarization simultaneously using a focal plane polarimeter, as discussed in Sec. 3.8. Because of the spin precession in the spectrometer magnetic field, the longitudinal and normal components get mixed. We have chosen a kinematic point in which there is maximum sensitivity to the longitudinal polarization and therefore no sensitivity to the normal component, in order to optimize our well-defined test of the two reaction mechanisms for $A_{LL}$ (Fig. 7) and extract $R_A$. The measurement of $A_{LT}$ is not affected by the spin precession. We propose to measure both $A_{LL}$ and $A_{LT}$, each with a precision of $\pm0.1$.

## 2.5 Goals of the Experiment

We propose measurements of cross sections in the energy range 3-6 GeV ($s$=6.1-11.5 GeV$^2$) and angular range $\theta_{cm}$=60°-135° ($-t$ up to 6.5 GeV$^2$) (see Fig. 8), with an expected statistical precision of 5% and systematic uncertainty in the absolute cross sections of about 6%. Our specific goals are as follows.

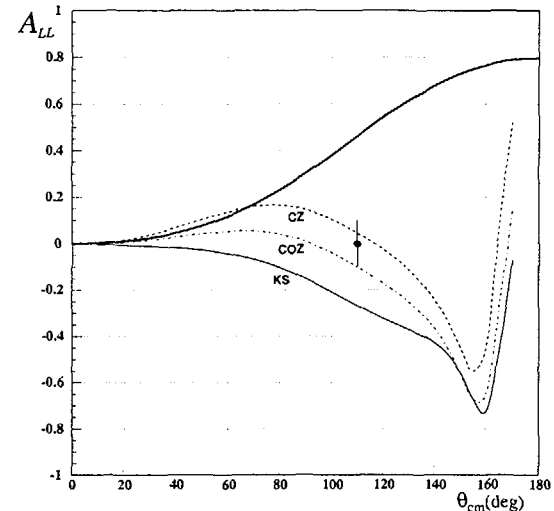1. Measure the scaling power $n(\theta)$ in the angular range $\theta_{cm} = 70° - 110°$ (see Fig. 3).



Figure 7: *Longitudinal polarization transfer parameter $A_{LL}$ at 4 GeV. The solid curve is the prediction based on the handbag mechanism with the form factors shown in Fig. 4. The other curves are pQCD calculations with various DA's. The point and error bar shows the projected precision from the present proposal.*

2. Test the approximate $s$-independence of the ratio $\sigma/\sigma_{KN}$ at fixed $t$ in the range $-t = 2.0-6.5$ GeV$^2$ and E= 3 − 6 GeV (see Fig. 6).

3. Measure the form factor $R_V(t)$ in the range $-t = 2.0 - 6.5$ GeV$^2$, with precision ranging from about 2% on the low side to about 10% on the high side (see Fig. 4).

4. Test qualitative predictions for the longitudinal and transverse components of the recoil polarization at $-t = 4$ GeV$^2$ (see Fig. 7).

5. Determine the form factor $R_A$ at $-t = 4$ GeV$^2$ by measuring the polarization transfer observable $A_{LL}$ to a precision of $\pm0.1$ (see Fig. 4).

6. Determine the form factor $R_T$ at $-t = 4$ GeV$^2$ by measuring the polarization transfer observable $A_{LT}$ to a precision of $\pm0.1$.

where $f_V$ is a kinematic factor given by

$$f_V = \frac{(\tilde{s} - \tilde{u})^2}{2(\tilde{s}^2 + \tilde{u}^2)} \tag{8}$$

and $\tilde{s} = s - m^2$ and $\tilde{u} = u - m^2$. As remarked above, the new physics is contained in the form factors, $R_V$ and $R_A$, which have a simple physical interpretation. The combination $|R_V(t) + R_A(t)|^2$ is the probability that a photon can scatter elastically from the proton by transferring $t$ to a single active quark whose helicity is oriented in the direction of the proton helicity. Similarly $|R_V(t) - R_A(t)|^2$ is the probability that the active quark has helicity opposite to that of the proton. Eq. 7 is analagous to the cross section for elastic electron scattering, except that the KN cross section replaces the Mott cross section. An interesting feature is that despite the similarity between the Compton scattering form factors (Eq. 6) and electron scattering form factors (Eq. 4), there are important distinctions. First, the weighting by the quark charge is quadratic in the former case and linear in the latter. Thus RCS is sensitive to the flavor structure of the proton in a different way than electro-weak scattering, thereby potentially providing another tool, along with parity-violating electron scattering, for decomposing the flavor structure. Second, the RCS form factors have an additional $1/x$ in the integral, giving rise both to a different weighting of momentum fraction and to an overall enhancement relative to the electron scattering form factors. Both the $e_a^2$ weighting and the $1/x$ factor lead to a sensitivity to sea quarks that is greater for RCS than for electron scattering form factors. Another interesting feature is the sensitivity of RCS to the axial structure of the nucleon through $R_A$, which is a topic of high current interest in the context of the flavor decomposition of the spin-dependent structure functions.

Radyushkin and Diehl et al. have modeled the ND's in order to predict cross sections. In their models

$$
\begin{aligned}
\mathcal{F}^a(x, t) &= f_a(x) \exp\left[\frac{(1-x)t}{4x\lambda_a^2}\right] \\
\mathcal{G}^a(x, t) &= \Delta f_a(x) \exp\left[\frac{(1-x)t}{4x\lambda_a^2}\right],
\end{aligned} \tag{9}
$$

where the factor $\lambda_a$ is related to the average transverse momentum $< k_\perp^2 >$ carried by the quarks of flavor $a$ in the proton. The helicity flip ND's $\mathcal{K}^a$ and $\mathcal{P}^a$ have not yet been modeled. Radyushkin [6] finds good agreement with the $F_1(t)$ data for $-t$ in the range 1-10 GeV$^2$ by adjusting $\lambda_a^2$ to 0.7 GeV$^2$, implying $< k_\perp^2 > \approx (300$ MeV$)^2$. This allows a prediction for the RCS form factors, which are shown in Fig. 4. An interesting feature of these form factors is that they decrease approximately as $1/t^2$ in the few-10 GeV$^2$ range, leading to $n \approx 6$ scaling factor, in agreement with asymptotic scaling. However, the handbag treatment of factorization predicts non-trivial violations of $n = 6$ scaling in the form of an angle-dependent scaling factor $n(\theta_{cm})$, which are in agreement with the existing (limited) data but which will be tested with good precision in the proposed experiment. Another intersting feature is that at sufficiently high $-t$, the exponential factor forces the integrand to be concentrated near $x = 1$, where the the parton distribution functions vary approximately as $(1 - x)^3$. This is the so-called Feynman mechanism [13] and it leads to an asymptotic behavior of $1/t^4$ for the form factors and therefore to $n \approx 10$. Thus the handbag contribution to RCS will be asymptotically subdominant to the hard gluon mechanism, even though the handbag is still expected to dominate at experimentally accessible energies.

In order to measure $R_V$ and $R_A$, it is necessary to measure the RCS cross section at fixed $t$ with a variable $f_V$ in order to achieve a "Rosenbluth-like" separation. Note that $f_V$, which assumes
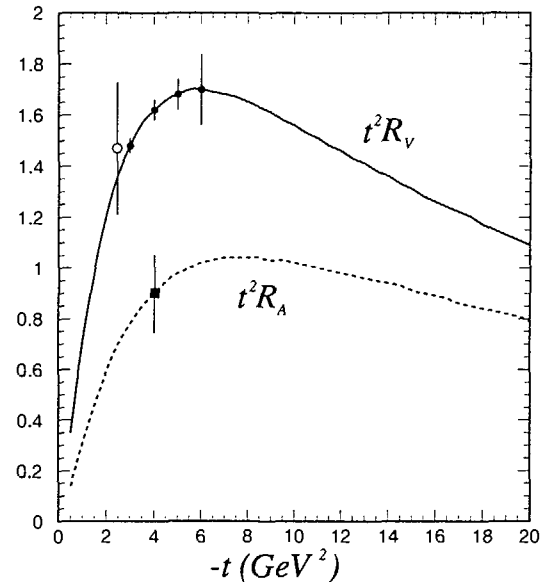


Figure 4: *Calculations of the RCS form factors $t^2 R_V(t)$ (solid line) and $t^2 R_A(t)$ (dashed line). The closed points and error bars show the projected precision from the present proposal. The open point is the result of a fit to the Cornell data. The square is the projected precision for $R_A$ based on the measurement of $A_{LL}$.*

values between about 0.5 and 1, depends principally on the scattering angle $\theta_{cm}$ and only weakly on energy, as shown in Fig. 5. For the kinematics of interest, where $s$, $-t$, and $-u$ are all large, $f_V$ is always close to 1. Consequently the unpolarized cross sections are largely insensitive to $R_A$. This leads to the very nice feature that the left-hand-side of Eq. 7 is nearly $s$-independent at fixed $t$, allowing a very powerful test of the reaction mechanism that we propose to test. In addition, the cross sections should allow a precise measurement of $R_V$, although $R_A$ will be nearly unconstrained. These features are demonstrated in Fig. 6, which shows data expected from this experiment. Also shown are the limited Cornell data at $-t=2.45$ GeV$^2$, which is probably at the edge of validity of the reaction mechanism.

## 2.4 Polarization Observables

A measurement of polarization observables provides further tests of the reaction mechanism as well as access to additional form factors. In this section we discuss the observables $A_{LL}$, $A_{LT}$, and

backgrounds, and systematic errors. The specific request for beam time is presented in Section 4. This proposal extends and supercedes E97-108, which was approved by PAC13.

# 2 Physics Motivation

## 2.1 Overview

In view of the remarks in the Introduction, we consider several interesting questions that motivate us to develop an experimental program of wide-angle real Compton scattering at JLab:

1. At what kinematic scale is factorization into hard and soft processes valid?

2. What is the dominant hard scattering mechanism at JLab energies?

3. What insights into the structure of the proton can be learned from new and precise RCS measurements?

4. What is the relationship between structure revealed from RCS and that from other reactions, such as elastic form factors, parton densities, etc.?

We concentrate our discussion on the pQCD and soft overlap mechanisms, since these represent the two extreme views of the hard scattering process.

## 2.2 pQCD Mechanism

In the pQCD mechanism, shown schematically in Fig. 1-a, there are three active quarks and the transferred momentum is shared among them by the exchange of two hard gluons. This leads naturally to the asymptotic quark counting rule and scaling [12],

$$\frac{d\sigma}{dt} = \frac{f(\theta_{cm})}{s^n}, \qquad (2)$$

where n=6 for RCS. Higher Fock states require additional gluon exchanges and are therefore suppressed by additional factors of $1/s$. For the pQCD mechanism, Eq. 1 takes the schematic form

$$T^{\mu\nu}(s,t) = \int d^3x d^3y \phi(x) \hat{K}^{\mu\nu}(x,y,s,t)\phi(y), \qquad (3)$$

where $\hat{K}^{\mu\nu}(x,y,s,t)$ is the hard scattering amplitude that includes all distinct diagrams in which two photons couple to three quarks which exchange two perturbative gluons. The soft physics is contained in $\phi(x_1,x_2,x_3)$, the valence quark distribution amplitude (DA), which is related to the 3-quark light-cone wave function of the proton and from which the parton densities can be obtained. Vanderhaeghen [3] has outlined a procedure of parametrizing the DA as a sum of polynomials, with coefficients adjusted to fit RCS data. Therefore, in the kinematic regime where the pQCD mechanism dominants, precise measurements of RCS cross sections can determine the DA.

Experimentally, the Cornell data [11] support scaling with $n \approx 6$ (see Fig. 2 and 3), albeit with modest statistical precision. Nevertheless, this does not necessarily mean that pQCD is the dominant mechanism. Indeed, as shown in Fig. 2, when Eq. 3 is evaluated with the symmetric DA, $\phi \sim x_1 x_2 x_3$, the cross section badly underpredicts the data. A similar story holds for the proton elastic form factor, where the symmetric or even slightly asymmetric DA's lead to a form factor
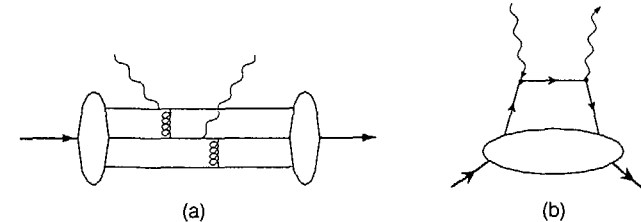


Figure 1: *Different hard scattering mechanisms for RCS. The small dots represent hard scatterings whereas the blobs represent soft interactions. In the pQCD mechanism (a), the momentum is shared among the quarks by hard gluon exchange. In the handbag diagram of (b), the scattering is from a single quark and the momentum is shared by the overlap of the high momentum components of the soft wave function.*

well below the data [8]. This can be alleviated somewhat using strongly asymmetric DA's [3], as shown in Fig. 2. However, in this case the integral is dominated by the endpoints, corresponding to the exchanged gluons close to their mass shell and therefore nonperturbative. This calls into question the internal consistency of the pQCD approach at moderate $s$ and $t$ [6, 8].

We propose to test whether the pQCD mechanism is the dominant one in the kinematic range accessible to JLab in two different ways. First, we propose precise measurements of the scaling factor $n(\theta)$, especially in the region near $\theta=90°$, since that is where $p_\perp$ is largest and therefore where the pQCD mechanism might be expected to work best. Our expected precision is shown in Fig. 3 for the angles 70°, 90°, and 110°. Second, we propose a single measurement of the longitudinal polarization transfer parameter $A_{LL}$, but we postpone a discussion of this until Sec. 2.4.

## 2.3 Soft Overlap (Handbag) Mechanism

Radyushkin [6] and subsequently Diehl *et al.* [7] suggest that the dominant mechanism at experimentally accessible energies for both elastic form factors and RCS is the soft overlap mechanism, where the handbag diagram (see Fig. 1-b) dominates and $t$ is absorbed on a single quark and shared by the overlap of high momentum components in the soft wave function. The important nonperturbative physics is contained in the wave function describing how the active quark couples to the proton. Radyushkin describes this coupling with four nonforward parton densities (ND): $\mathcal{F}^a(x;t)$, $\mathcal{G}^a(x;t)$, $\mathcal{K}^a(x;t)$, and $\mathcal{P}^a(x;t)$, corresponding to vector, axial vector, tensor, and pseudoscalar couplings, where $a$ labels the quark flavor. The ND is the superstructure that links inclusive (e.g., parton densities) to exclusive (e.g., elastic form factors) structure. For example

$$F_1(t) = \Sigma_a e_a \int_0^1 \mathcal{F}^a(x;t)dx$$

$$G_A(t) = \Sigma_a e_a \int_0^1 \mathcal{G}^a(x;t)dx$$